A Patient-Specific Correspondence Model to Track Tumor Location in Thorax during Radiation Therapy

A DISSERTATION

SUBMITTED TO THE FACULTY OF THE GRADUATE SCHOOL OF THE

UNIVERSITY OF MINNESOTA

BY

Sharareh Fakhraei

IN PARTIAL FULFILLMENT OF THE REQUIREMENTS FOR THE DEGREE OF

DOCTOR OF PHILOSOPHY

Parham Alaei, Ph.D.

May, 2021

Acknowledgements

I would like to express my gratitude to my advisor, Dr. Parham Alaei, for all his guidance and support during these past five years. His knowledge, mentorship skills, new ideas, and constant encouragement have made my graduate study a rich and memorable journey. He has set me an example of excellence as a mentor, instructor, and medical physicist.

I would like to thank David Sterling and Dr. Eric Ehler for their help and insightful comments on the technical aspects of this project. I would like to thank Dr. Chinsoo Cho for his efforts with the patient study. I would also like to thank the radiation therapy technologists at the University of Minnesota Medical Center for their help with patient data acquisition.

I like to especially thank my husband, Ali. His endless love, support, and encouragement made this dissertation possible. Finally, I would like to truly thank my family for all their support and encouragement throughout my life.

Dedication

For my husband, Ali.

Abstract

In radiation therapy of tumors in the thorax and abdomen, respiratory-induced motion creates challenges in different steps of the treatment, such as simulation, treatment planning, and the daily patient positioning. Different methods are clinically applied to reduce the impact of respiration in radiation therapy. However, most techniques involve invasive procedures or expose the patient to extra radiation. In this thesis, first, the application of combining stereotactic body frames with a surface imaging system for patient positioning in stereotactic body radiotherapy (SBRT) of lung cancer was evaluated. Stereotactic body frames are safe and non-invasive devices that reduce the impact of respiratory-induced motions by decreasing the range of the tumor motion. Surface imaging systems are also safe and dose-free technologies for patient positioning that have the ability to monitor the patient's motion during radiation delivery with high precision. Combining the use of a surface imaging system with SBRT positioning frames adds another level of accuracy to patient setup and provides monitoring of the movements during treatment. The results of this evaluation indicated difficulty in using surface imaging with SBRT frames primarily due to the presence of the compression plate.

Next, a patient-specific correspondence model was developed to track tumors in the thorax during radiation therapy treatments using surface displacement as the surrogate signal. The proposed model is made prior to the treatment for each patient. Two types of data are used for model construction: Four-dimensional computed tomography (4DCT) images of the patient and the displacement of two points on the patient's skin on the thoracic area

(surrogate signals). The two types of data are acquired simultaneously. The 4DCT images are sorted by the amplitude-binning algorithm to account for hysteresis and breathing irregularities. A deformable image registration algorithm is applied to the 4DCT images to calculate the deformation vector fields as the knowledge of the patient's internal motion. Principal component analysis is used to fit the correspondence model. The model incorporates recorded surrogate signals during radiation delivery as an input and delivers the 3D trajectory of the tumor or other anatomy of the interest. This model accounts for hysteresis and irregular breathing. The accuracy of the proposed model was evaluated on a respiratory phantom and five lung cancer patients. The results showed a primary validation for localizing the tumors in the lung. Testing the model on a larger population of patients will examine the accuracy of the localization more precisely.

Table of Contents

Acknowledgements ..... **i**

Dedication ..... **ii**

Abstract ..... **iii**

List of Tables ..... **viii**

List of Figures ..... **ix**

List of Abbreviations ..... **xiv**

1. Introduction **1**

1.1. Motion Management in Radiation Therapy **1**

1.1.1 Motion Encompassing Methods 2

1.1.2 Respiratory Gating Methods 3

1.1.3 Breath-Hold Methods 5

1.1.4 Forced Shallow Breathing with Abdominal Compression 7

1.1.5 Real-Time Tumor Tracking Methods 7

1.2. Surface Guided Radiation Therapy **11**

1.2.1. Video-Based Positioning Systems 11

1.2.2. Laser-Based Positioning Systems 12

1.2.3. Optical-Based Positioning Systems 13

1.3. Goals of the Study **18**

2. Evaluation of Combining CatalystHD with Stereotactic Body Frames for Patient Positioning in Lung Radiation Therapy **19**

2.1. Introduction 19

2.2. Materials and Methods 20

2.3. Results 22

2.4. Conclusion 25

3. A Patient-Specific Correspondence Model to Track Tumor Location in Thorax during Radiation Therapy 26

3.1. Introduction 26

3.2. Materials and Methods 30

3.2.1. Data Acquisition for Model Construction 32

3.2.2. Surrogate signal Processing 35

3.2.3. 4DCT Image Processing 39

3.2.4. Constructing the Correspondence Model 43

3.2.5. Surrogate Signals as the Model Input 45

3.2.6. Respiratory Phantom 46

3.2.7. Patient Data 50

3.3. Results 58

3.3.1. Respiratory Phantom 58

3.3.2. Patient Data 59

3.4. Discussion 64

3.5. Conclusions 66

4. Summary and Future Work 67

4.1. Summary 67

4.2. Future Work 68

Bibliography 70

Appendix A 84

List of Tables

Table 3-1. Characteristics of the patients in the study. 50

Table 3-2. The magnitude of the average and standard deviation of the displacement in each direction compared with the ground truth for respiratory phantom. 59

Table 3-3. The average and standard deviation of the tumor center or diaphragm apex displacement during treatment in LR direction calculated by the model for each patient compared with the ground truth. 61

Table 3-4. The average and standard deviation of the tumor center or diaphragm apex displacement during treatment in AP direction calculated by the model for each patient compared with the ground truth. 62

Table 3-5. The average and standard deviation of the tumor center or diaphragm apex displacement during treatment in SI direction calculated by the model for each patient compared with the ground truth. Number of the respirations indicates the number of respirations used to calculate the ground truth. This is the number of all consecutive EE and EI projections for which the tumor center or the apex of the diaphragm was visible to the eyes. 62

Table 3-6: Systematic uncertainty for each step of the model construction and the calculated total systematic uncertainty. 63

List of Figures

Figure 1-1. A schematic view the locations of the cameras in video-based positioning system (figure from Milliken et. al. 1997 [54]) 12

Figure 1-2. Sentinel. The laser scanner scans the patient's surface while the camera detects the reflection of the laser from patient's surface. (figure courtesy of C-RAD). 13

Figure 1-3. An image of the AlignRT unit (a) and the visualization of three AlignRT units mounted on the ceiling of the radiation treatment room (b) (figure from Alaei and Ding (Eds.), 2018 [58]). 14

Figure 1-4. An image of the CatalystHD unit (a) and the visualization of three CatalystHD units mounted on the ceiling of the radiation treatment room (b) (figure courtesy of C-RAD). 16

Figure 1-5. Illustration of IDENTIFY units in treatment room (figure courtesy of Varian). 17

Figure 2-1. A anthropomorphic Rando phantom covered with a white sheet in order to be visible to the SIGRT cameras. The phantom was positioned on a Vac-Lok vacuum cushion. 21

Figure 2-2. Illustration of phantom setup on the treatment room using Bionix Omni V stereotactic body frame and compression plate (a), and the surface image recorded by CatalystHD (b). 22

Figure 2-3. Illustration of phantom setup on the treatment room using Bionix Omni V stereotactic body frame and respiratory belt (a), and the surface image recorded by CatalystHD (b). 23

Figure 2-4. Illustration of phantom setup on the treatment room using Civco body Pro-lok stereotactic body frame and compression plate (a), and the surface image recorded by CatalystHD (b). 23

Figure 2-5. Illustration of phantom setup on the treatment room using Elekta Body Frame stereotactic body frame and compression plate (a), and the surface image recorded by CatalystHD (b). 24

Figure 3-1. Demonstration of how a correspondence model is typically made (figure from Ehrhardt and Lorenz (Eds.), 2013[75]). 28

Figure 3-2. A simple representation of the framework of the proposed correspondence model. The model calculates the location of the center of the tumor in three directions, Left-Right (LR), Anterior-Posterior (AP), and Superior-Inferior (SI), during the treatment. 31

Figure 3-3. Illustration of the surface image of the patient no. 3 in the study recorded by Sentinel on the simulation day. The location of the primary and secondary signals is shown on the surface image. 32

Figure 3-4. Primary and secondary signals recorded for patient no. 3 in the study. The 4DCT acquisition period is identified by red on the signals. 33

Figure 3-5. Illustration of phase-binning algorithm (a) and amplitude-binning algorithm (b) on the respiratory signal. 34

Figure 3-6. 4DCT period of the primary and secondary signals for patient no. 3 in the study. The original signals is shown in blue and the signals after pre-processing step is shown in red. 36

Figure 3-7. For calculation of average amplitude of each respiratory phase, after identifying all the minima and maxima on each signal, the average amplitude of maxima and the average amplitude of all minima were calculated and set as extremities (signals in the image from patient no. 3 in the study). 37

Figure 3-8. After calculation of the amplitude of EI (0%) and EE (50%) phases, to calculate the amplitude of the remaining respiratory phases, four points at equal distances divided the interval between the calculated 0% and 50% average amplitudes (signals in the image from patient no. 3 in the study). 38

Figure 3-9. Illustration of calculated average amplitude of each respiratory phase for patient no. 3 in the study. 39

Figure 3-10. Illustration of a schematic view of DVFs resulting from registration of EI (or 0%) and EE (or 50%) phases on the coronal view of one of patient no. 4 in the study. The image on the left is the moving image (EI) and the image on the right is the fixed image (EE). 41

Figure 3-11. Illustration of primary and secondary signals recorded on the treatment day for patients no. 3 in the study. 46

Figure 3-12. CIRS Xsight Lung Tracking Phantom kit. 47

Figure 3-13. A CIRS Xsight Lung Tracking Phantom as positioned on the CT scanner couch. A large skin-like silicone pad was placed on the phantom to cover the surrogate platform and connect it to the phantom. 48
Figure 3-14. A CIRS Xsight Lung Tracking Phantom as positioned on the linear accelerator couch. A large skin-like silicone pad was placed on the phantom to cover the surrogate platform and connect it to the phantom. The red and light green circles on the silicon pad represent the position of primary and secondary signals, respectively. 49
Figure 3-15. The logarithmic 2D projection of one of patient no.3 in the study in EE phase after applying a threshold..... 52
Figure 3-16. The derivative of the image in Figure 3-15 is taken in the SI direction using a Sobel gradient operator. 53
Figure 3-17. Applying a threshold to the image in Figure 3-16 (left) and it projection on craniocaudal axis at the (right). 54
Figure 3-18. The Amsterdam Shroud image constructed for one of the patients in the study. 55
Figure 3-19. Diaphragm region was cut from the AS image (a). Diaphragm region is collapsed onto the temporal (horizontal) axis by summing over all pixel intensity values in each column (b). The respiratory signal is obtained after applying a high-pass filter. Each red point on the signal is representing a projection (c). 56
Figure 3-20. Location of the target sphere centroid calculated by the model for the respiratory phantom. The direction of the motion matches the true direction of the centroid motion along all three axes. 58

Figure 3-21. PCA eigenvalue spectrum for the respiratory phantom (a) and for patient no. 5 (b). 59

Figure 3-22. Location of the left diaphragm apex during the radiation delivery calculated by the model for patient no. 5 in the study. 60

List of Abbreviations

3D	Three dimensional
4D	Four dimensional
4DCT	Four dimensional computed tomography
6D	Six dimensional
AP	Anterior-posterior
AS	Amsterdam shroud
CBCT	Cone beam computed tomography
CT	Computed tomography
CTV	Clinical target volume
DIBH	Deep-inspiration breath hold
DIR	Deformable image registration
DOF	Degree of freedom
DVF	Deformation vector field
EE	End of exhalation
EI	End of inhalation
FOV	Field of view
FSB	Forced shallow breathing
IGRT	Image-Guided radiation therapy
IMRT	Intensity modulated radiation therapy
IRB	Institutional Review Board
LINAC	Linear accelerator
LR	Left-right
mDIBH	Moderate deep-inspiration breath hold
MLC	Multi-leaf collimator
PCA	Principal Component Analysis

PTV	Planning target volume
RCCT	Respiratory correlated computed tomography
RMSE	Root mean square error
SABR	Stereotactic ablative radiotherapy
SBF	Stereotactic body frame
SBRT	Stereotactic body radiation therapy
SGRT	Surface guided radiation therapy
SI	Superior-inferior
MIP	Maximum intensity projection

Chapter 1

1.Introduction

1.1. Motion Management in Radiation Therapy

Recent advances in modern radiation therapy have resulted in delivering a more focused beam to the tumor with a sharp radiation dose gradient [1]. Therefore, to deliver the maximum radiation dose to the tumor while sparing the organs at risk and healthy tissues, a precise measure of the tumor location is critical. Image-Guided radiation therapy (IGRT) uses imaging techniques to localize and monitor the location of the target volume before and during the radiation treatment. Inter-fraction errors and intra-fraction motions are the main factors that affect the location of the target volume. Inter-fraction errors are variations in target location that take place in day-to-day treatments. Intra-fraction motions are the movements of the target during radiation treatment that are usually caused by the respiratory, cardiac, muscular, and gastrointestinal systems. Respiratory-induced motion, however, remains one of the challenges in IGRT, and many studies have been undertaken to solve the treatment delivery limitations that arise by motions due to respiration. For imaging of the tumors in the thorax and abdomen, respiratory motion reduces the image quality and causes artifacts [2], [3]. The respiratory motion also affects the accuracy of treatment planning [4], dose calculations [5], and quality of the radiation delivery.

In treatment planning, margins are added to the clinical target volume (CTV) to account for respiratory motions. However, this means a larger field size is needed, and as a result, more healthy tissue will receive high radiation doses [6].

There are suggested methods to decrease the effect of respiratory motion. All methods are described below in detail using the classification provided by AAPM Task Group 76 [6].

1.1.1 Motion Encompassing Methods

One of these methods is motion-encompassing. In this method, the target's mean position and range of motion are assessed while computed tomography (CT) imaging. Three techniques that are used to estimate the target's range of motion include slow CT scanning [7]–[9], Inhalation and exhalation breath-hold CT [2], [10], [11], and four dimensional computed tomography (4DCT)/respiratory correlated CT (RCCT) [12]–[16]. In the slow CT scanning technique, the CT scanner is running very slow such that more than one respiration phases are recorded in each slice. Therefore, the target's full range of motion should be apparent in the CT image. However, since the respiratory motion might change from simulation day to treatment day, additional margins are required to compensate for these changes. One of the disadvantages of this technique is motion blurring. The slow scanning technique is usually used to scan peripheral lung tumors. But, due to motion blurring, it is not suitable for imaging the tumors that are near the mediastinum and/or chest wall. This technique is also not recommended for tumors other than lung tumors such as kidney, pancreas, or liver.

One of the common techniques to estimate the target's range of motion is inhalation and exhalation breath-hold CT. In this technique, on the simulation day, both inhalation and exhalation-gated or breath-hold CT scans are acquired from the patient. Since two scans are acquired, image fusion and additional contouring are needed. The maximum intensity projection (MIP) [17] tool, which is available in many of the visualization systems, is utilized to acquire the tumor-motion-encompassing volume for lung tumors. Acquiring both inhalation and exhalation scans takes more than double the CT scanning time, and depends on the patient's ability to hold his/her breath reproducibly. However, in this technique, the motion blur is less than slow scanning technique.

The third technique in the motion-encompassing method is 4DCT or RCCT. The tumor's mean position, range of motion, and characteristics of the motion [15] can be calculated from the 4D data. Variations in the respiratory pattern during 4D image acquisition may cause artifacts. Methods such as breathing-training are developed [18] to solve the respiratory pattern variation limitation; however, artifacts may still be seen [19].

All of the techniques that are mentioned above increase the radiation dose to the patient by 2-15 times that of a standard CT simulation procedure.

1.1.2 Respiratory Gating Methods

Respiratory gating methods decrease the impact of respiratory motion. In respiratory gating, the radiation is delivered in a specific portion of the patient's respiratory cycle, which is called the "gate." Respiratory gating is performed both during imaging and treatment delivery. The patient's respiratory motion is monitored by an external respiratory

signal or an internal fiducial marker to determine the position and the width of the gate within the respiratory cycle. In gated techniques, the imaging or treatment procedures' time increases since the radiation delivery is not continuous. However, one of the advantages of the gated methods is that the planning target volume (PTV) margins could be decreased since the imaging and treatment procedures are synchronized with the patient's respiratory cycle.

Two variables are defined for respiratory motion, amplitude and phase, and they are recorded through the respiratory signal or the internal anatomy motion. Thus, gating methods are divided into two categories; amplitude-gating, and phase-gating. The amplitude of the respiration signal is measured as the relative position of the signal between end-inhalation and end-exhalation. In amplitude-gating, the radiation delivery is performed each time the respiratory signal is within a preset window of relative positions. The phase of the respiration signal is calculated from the respiratory signal by an algorithm that must meet the frequency criteria. Each complete respiration is considered as a phase interval between 0 and 2π, with 0 as the end of inhalation and π as the end of exhalation. In the phase-gating, the radiation delivery is performed each time the respiratory signal is within a preset phase window.

Usually, the gate window covers that part of the respiratory cycle that tumor's motion is estimated to be less (i.e., end of exhalation) or the part of the respiratory cycle that the lung's volume is maximum (i.e., end of inhalation).

The efficiency of the gating method is measured by the duty cycle. The duty cycle is defined as the ratio of beam-on time to the entire treatment time. Smaller duty cycle leads

to smaller treatment margins. However, the overall treatment time increases, and this increases the likelihood of patient motion due to discomfort [20].

Despite gating, there is still some tumor motion within the gate window which is called residual motion [21]. The choice of gate width is generally compromised by the balance between the amount of residual motion and duty cycle.

1.1.3 Breath-Hold Methods

The third series of methods to reduce the effect of respiratory motion are breath-hold methods. These methods are commonly used in lung cancer radiotherapy, and they also have some advantages in breast cancer radiation therapy. Breath-hold methods include five types of techniques, deep-inspiration breath hold (DIBH) [22]–[24], active breathing control (ABC) [25], [26], self-breath hold without respiratory monitoring [27], [28], self-breath hold with respiratory monitoring, and breath hold in combination with intensity modulated radiation therapy (IMRT).

Deep-inspiration breath hold can efficiently reduce the tumor motion in the thorax. A deep-breath hold usually can alter the anatomy in a way that healthy organs at risk are protected. In the DIBH technique, the patient is verbally coached to a reproducible state of deep inhale breath hold both on simulation day and treatment day. One of the DIBH limitations is that many of the patients are not able to repeat the breath-hold reproducibly enough to permit its use.

Active breathing control technique eases the reproducibility of the breath-hold. In this technique, the air flow during the respiratory cycle is monitored by a spirometer. The air

flow stops at a preset threshold volume by the ABC apparatus, and this helps the patients to maintain their breath at this volume [26], [29]. The duration of breath-hold depends on the patient, but it is usually between 15 and 30 seconds.

The choice of threshold volume is usually either moderate inhale or deep inhale. In moderate DIBH (mDIBH), the threshold volume will be set at 75% of deep inhale. This increases the reproducibility of the internal organ displacement and also retains the patient's comfort [25], [30], [31].

In self-breath hold without respiratory monitoring technique, the patient holds their breath at a specific point in the respiratory cycle and simultaneously enable the treatment beam by pushing a switch connected to a control system. This allows the therapist to activate the radiation beam. The beam can be turned off by both the patients (when they aims to stop holding their breath) and the therapist. Based on previous studies, deep inhalation and deep exhalation are the most reproducible states of respiration. However, since deep inhalation has dosimetric advantageous due to the reduction in lung density, deep inhalation is usually the choice of the breath-hold position [22].

In self-breath hold with respiratory monitoring technique, the patient holds his/her breath at a specific point in the respiratory cycle; however, the patient's respiration is monitored continuously. If the patient's breath-hold level deviates from the preset level, the beam will be stopped.

1.1.4 Forced Shallow Breathing with Abdominal Compression

Forced shallow breathing (FSB) was first developed for stereotactic radiation therapy of small targets in the lung and liver [32]–[34]. However, it also could be used for conventional lung treatments. In this technique, a stereotactic body frame (SBF) is used to immobilize the patient. The SBF consists of a rigid frame and a vacuum pillow. The vacuum pillow is costom fitted to each patient. A compression plate is attached to the frame that is pressed against the abdomen to limit the diaphragmatic motion. A bar is attached to the SBF to support the compression plate.

On the simulation day, the motion of the tumor in the craniocaudal direction is evaluated by a fluoroscopic simulator. If the motion of the tumor exceeds 5 mm, the compression plate is put on the patient's abdomen in a way that the two upper angled sides of the plate are placed at 2 – 3 cm below the triangular rib cage. The position of the bar connected to the compression plate is recorded from the scales on both sides of the frame to be reproduced on the treatment day. The position of the plate is also reproduced by recording the scale mark on the screw that controls the location of the plate.

1.1.5 Real-Time Tumor Tracking Methods

Another method to reduce the impact of the respiratory motion is real-time tracking. In real-time tracking, the radiation beam's position is changing dynamically to follow the tumor's position. An ideal real-time tracking can reduce the treatment margins substantially. A successful real-time tracking must be able to do four things:

a) recognizing the location of the tumor in real-time,

b) predicting the motion of the tumor to permit for the time delays that beam-positioning system needs to respond,
c) repositioning the radiation beam,
d) Tuning the dosimetry in order to follow the variation of the lung volume and location of the critical organs during respiration.

In real-time tumor tracking, the most challenging step is identifying the location of the tumor. One way to track the tumor position during radiation delivery is imaging the tumor by an imaging modality such as fluoroscopy. However, for most tumors in the lung, liver, and pancreas, it is only possible to detect the tumor in fluoroscopy (or radiographic) images in specified positions. And, the detected tumor is not always a high contrast object that can be used in automatic segmentation or image registration. Therefore, fiducial markers are implanted in lung, liver, or pancreas tumors [35]–[38]. Markers are usually made from one of the high-Z metals (e.g., gold). The number of markers implanted in a tumor is often more than three. More than three markers not only allow the measurement of both translation and rotation of the tumor, but it also helps to monitor the possible migration of the markers by measuring the distance between them. Real-time tracking with imaging causes extra radiation dose to the patient. Therefore, a combination of episodic x-ray imaging and continuous monitoring of external respiratory signals are suggested to reduce the exposure to the patient.

It is not always possible to track the tumor location continuously by x-ray imaging. An alternative is to estimate the position of the tumor from an external respiratory signal. The correlation between internal and external motion can be found before treatment. This

correlation is not always simple and stationary. Thus, the correlation should be monitored and updated during the treatment by respiratory signals and occasional imaging.

Another real-time tumor tracking technique is non-radiographic tracking of an active or passive device that is implanted in the tumor [39], [40]. In this technique, a powered radiofrequency coil is implanted inside the tumor. This coil could be tracked electromagnetically in three dimensions. The advantage of this technique is that it is dose-free and, therefore, could be a substitute to track tumors with x-ray imaging.

Compensating for time-delays in the beam-positioning response is another important characteristic that a real-time tracking technique should possess. Image acquisition, data readout, image processing needed to locate the marker, triggering the beam operation, and required time for beam repositioning all are obstacles to the instantaneous beam-positioning response. A 90 ms delay between marker recognition and the start of a gated radiation beam has been reported [41]. Therefore, there is a need to predict the location of the tumor in advance. Although there are variations in the cycle to cycle of human breathing, these variations are not purely random [42], and the tumor location can be predicted accurately by up to 80% [37].

For real-time tracking to be performed, there should be the possibility of beam repositioning. Currently, there are three beam repositioning systems, multi-leaf collimator (MLC) [43]–[47], robotic-arm-mounted linear accelerator (LINAC) [35], [36], [48], [49], and Gimbaled x-ray head [50]–[52]. In the second approach, an imaging system monitors the location of the tumor. The robotic-arm is coupled to the imaging system through a control loop that navigates the repositioning of the beam.

Respiratory-induced motion has an impact on both the quality and quantity of the radiation therapy dose distributions [53]. The images that are used for dosimetry in treatment planning are only an instant presentation of anatomies of the patient. However, during radiation delivery, there are continuous variations in anatomy and the air volume in the lungs. This will disturb the beam attenuation and also alter the relative location of the tumor, normal tissues, and critical structures. Although the impact of the respiratory-induced motion on dosimetry is small, its effect is still required to be studied.

1.2. Surface Guided Radiation Therapy

Surface guided radiation therapy (SGRT) is one of the rapidly growing modalities of IGRT. Surface guided technologies have significantly improved the accuracy of patient positioning and real-time tracking in radiation therapy. Surface imaging systems have several advantages. They are dose-free and non-invasive and can monitor the patient's position during the treatment. They also can monitor and record respiratory signal as surrogate to use in motion management strategies.

In surface guided techniques, a reference surface image of the patient is recorded on the simulation day. On the treatment day, a live surface image of the patient is registered to the reference image that is correlated to the isocenter of the radiation delivery system.

The main principle of surface imaging systems is stereophotogrammetry. In this technique, a 3D image is reconstructed from multiple 2D images with known spatial geometry information. Different types of surface imaging systems are explained below in detail.

1.2.1. Video-Based Positioning Systems

The video-based patient positioning technique was one of the first surface imaging approaches developed and clinically implemented [54]. In this technique, on the simulation day, after the patient was set up accurately, a reference image is acquired from the patient. On the treatment day, the reference image is subtracted from the real-time images of the patient during the patient setup. The basic system includes three wall-mounted cameras and one ceiling-mounted camera that provide a favorable large field of view (FOV) of the patient (Figure 1-1)

The video image subtraction approach provides a quick, easy to use, accurate, and intuitive way for patient positioning/setup in radiation treatment. Clinical experience of using video-based patient positioning system in head and neck radiotherapy showed setup error between 1 to 3 mm [55].

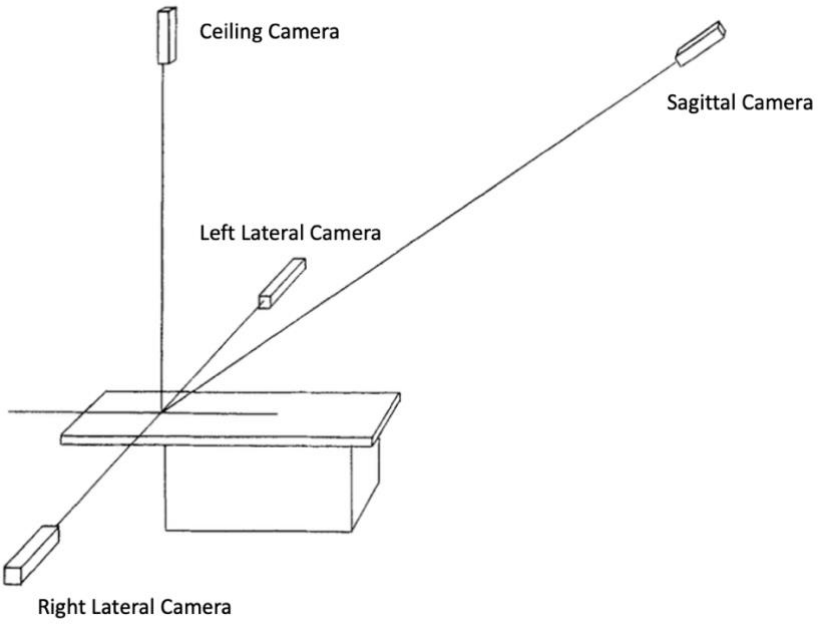

Figure 1-1. A schematic view the locations of the cameras in video-based positioning system (figure from Milliken et. al. 1997 [54])

1.2.2. Laser-Based Positioning Systems

Another approach developed for more accurate and reproducible patient positioning in radiation therapy employs a 4D laser scanning system to record the surface image of the patient [56]. This laser scanning system is now commercialized as Sentinel 4DCT (C-RAD

AB, Uppsala Sweden). Sentinel has a laser scanning system to scan the patient's surface and a camera to detect the reflection of the laser from the patient's surface (Figure 1-2). Sentinel is also capable of recording the respiratory surrogate signals, which can be used for 4DCT reconstruction and retrospective and prospective gating purposes.

Figure 1-2. Sentinel. The laser scanner scans the patient's surface while the camera detects the reflection of the laser from patient's surface. (figure courtesy of C-RAD).

Another commercially available laser-based positioning system is Galaxy (LAP Laser, Luneburg, Germany). The Galaxy's technology is similar to Sentinel, and a study on healthy volunteers shows that its lowest observed accuracy is between 1.70 to 0.15 mm [57].

1.2.3. Optical-Based Positioning Systems

The majority of commercially available patient positioning systems use optical cameras. In optical-based positioning systems, a structured pattern of light is projected on the patient's surface by a camera, and the reflection of the light from the patient's surface is

detected by another camera to reconstruct the patient's surface image. Then a 6D matching software measures the shifts between the real-time image and the reference image (which is captured on the simulation day).

One of the commercially available optical-based positioning systems is AlignRT (Vision RT, London, UK). In AlignRT technology, a camera projects a speckle pattern light on the patient's surface, and another camera detects the distortions of the known projected speckle light pattern (Figure 1-3.a). Both cameras are installed inside one unit and calibrated to the treatment isocenter. For a desirable field of view of the patient's surface in spite of gantry rotation, three units are mounted on the ceiling of the treatment room with 90-degree between the units (Figure 1-3.b).

Figure 1-3. An image of the AlignRT unit (a) and the visualization of three AlignRT units mounted on the ceiling of the radiation treatment room (b) (figure from Alaei and Ding (Eds.), 2018 [58]).

The reconstructed surface image consists of triangular surface tiles and, therefore, has the geometry information of the surface [59]. The reconstructed real-time surface images are registered to the reference image acquired on the simulation day or on the first treatment day using a 6D matching software. The matching software employs the iterative closest point (ICP) registration algorithm to find 6D correction vectors that match the reference image to the live image on treatment day. After setting up the patient accurately and matching the reference image isocenter with the treatment isocenter, the patient can be translated or rotated by up to 1 mm or 1 degree from the treatment isocenter [59], [60].

AlignRT cameras monitor the patient actively during the radiation delivery. AlignRT has a beam-hold interface feature. In this case, if the patient moves outside a pre-defined tolerance, the beam can be put on hold by the software.

Another commercially available optical-based positioning system is Catalyst HD (C-RAD AB, Uppsala Sweden). Each unit of the CatalystHD has a projector that uses a light-emitting diode (LED), and a detector camera consisting of a charge-coupled device (CCD) for the reflected light from the patient's surface [61] (Figure 1-4.a). In CatalystHD, optical visible light is projected on the patient's surface with a striped pattern. Depending on the geometry of the radiation delivery system, between one to four CatalystHD units can be mounted on the treatment room ceiling (Figure 1-4.b).

When the patient's surface is reconstructed, a 6D matching software employs a deformable image registration (DIR) algorithm to register the live image with the reference image. After setting up the patient accurately and matching the reference image isocenter with the

treatment isocenter, the patient can be translated or rotated by up to 1 mm or 1 degree from the treatment isocenter [62].

CatalystHD cameras monitor the patient actively during the radiation delivery. CatalystHD's beam-hold interface feature will put the radiation beam on hold if the patient moves outside a pre-defined tolerance. CatalystHD is capable of recording the respiratory surrogate signals, which can be used for gating purposes.

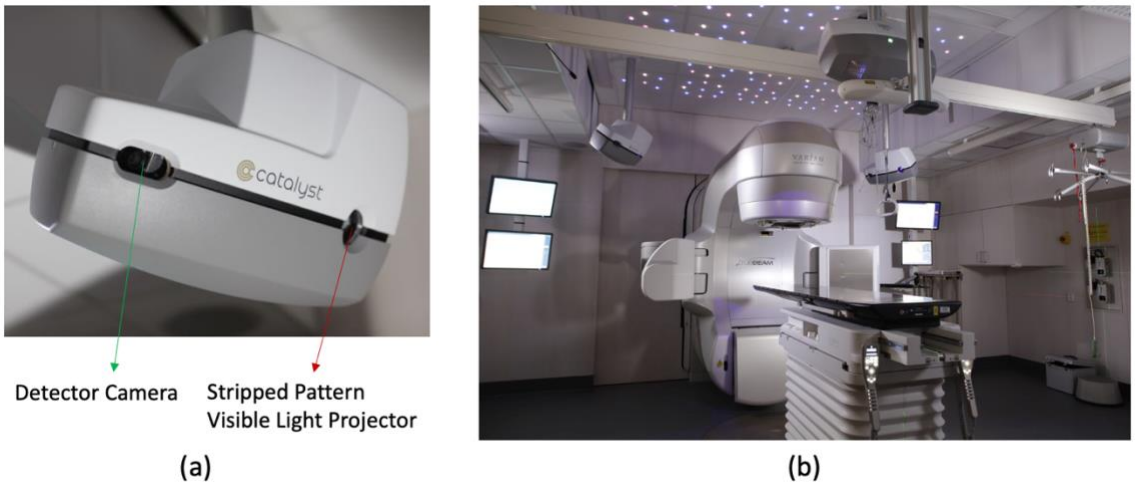

Figure 1-4. An image of the CatalystHD unit (a) and the visualization of three CatalystHD units mounted on the ceiling of the radiation treatment room (b) (figure courtesy of C-RAD).

IDENTIFY (Varian Medical Systems, Palo Alto, CA) is another commercially available optical positioning system (Figure 1.5). The basic technology of the IDENTIFY is the same as AlignRt and CatalystHD. Each Identify unit is consists of a projector and a pair of cameras for detecting the projected light from the patient's surface.

After surface reconstruction, a 6D matching software employs a rigid image registration algorithm to register the live image with the reference image. IDENTIFY can monitor the patient's movements during the treatment and can record the respiratory signals for gating treatments.

Figure 1-5. Illustration of IDENTIFY units in treatment room (figure courtesy of Varian).

1.3. Goals of the Study

The main goal of this project was to evaluate the use of surface guidance to decrease the impact of respiratory-induced motion in radiation therapy of lung cancer patients with the ultimate aim of reducing the use of x ray-based imaging. Chapter 2 discusses the possibility of combining the use of stereotactic body frames with surface guidance. Chapter 3 represents the development of a patient-specific correspondence model to track the tumors in the lung during radiation delivery. This chapter discusses the evaluation of the accuracy of the model on a respiratory phantom and several lung cancer patients. Chapter 4 summarizes the study and describes the possible future work.

Chapter 2

2.Evaluation of Combining CatalystHD with Stereotactic Body Frames for Patient Positioning in Lung Radiation Therapy

2.1. Introduction

In stereotactic body radiotherapy (SBRT) or stereotactic ablative radiotherapy (SABR), a focused radiation beam is delivered in a small number of fractions [63]. To reduce the target's treatment margins and, therefore, to spare the tumor's peripheral healthy tissues, two tasks are necessary: an accurate and reproducible patient positioning (minimizing the inter-fraction errors), and tracking the patient and the target's motions (intra-fraction motions).

Stereotactic body frames are used for patient immobilization and to reduce the motion during radiation therapy of lung tumors [32]. The application of the stereotactic body frame improves the accuracy of the radiation delivery by reducing the range of the tumor motion and increasing the reproducibility of the patient setup [64], [65].

Cone beam computed tomography (CBCT) images are conventionally used for patient positioning in radiation therapy. Although CBCT scans are currently the most accurate patient positioning techniques, they expose the patient to extra x-ray radiation. Moreover, CBCT scans cannot be utilized for tracking the intra-fraction motions.

Recently, surface imaging systems have been employed for patient positioning in radiotherapy. Not only are they dose-free, but they can also monitor the patient's movements during the radiation delivery. Studies have shown that surface imaging systems can detect patient positioning errors with good accuracy and reproducibility [66]–[69]. Therefore, the application of surface imaging systems can potentially decrease the frequency of CBCT scans [62].

In this section, the suitability of CatalystHD in combination with stereotactic body frames was investigated for patient positioning and intrafraction motion tracking in lung cancer radiation therapy.

2.2. Materials and Methods

Three commercially available immobilization systems were employed, Elekta Body Frame (Elekta AB, Stockholm, Sweden), Civco body Pro-lok (CIVCO Medical Solutions, Orange City, IA, USA), and Bionix Omni V (Bionix Development Corporation, Toledo, Ohio, USA) stereotactic body frame.

An anthropomorphic Rando phantom (Alderson Research Laboratories, Stanford, CT) was covered with a white sheet in order to be visible to the SIGRT cameras (Figure 2-1). After placing the phantom on a Vac-Lok (CIVCO Medical Solutions, Orange City, IA, USA)

vacuum cushion, the phantom and the cushion were both positioned inside each frame and setup on the Philips Brilliance Big Bore CT scanner's (Philips Medical Systems, Cleveland, OH) couch. The phantom was CT scanned, and a surface image was recorded using C-RAD Sentinel to create the reference image dataset. The CT images were exported to the Pinnacle treatment planning system (TPS) (Philips Radiation Oncology Systems, Fitchburg, WI), where external contours were generated and exported to the C-RAD system to use as reference images.

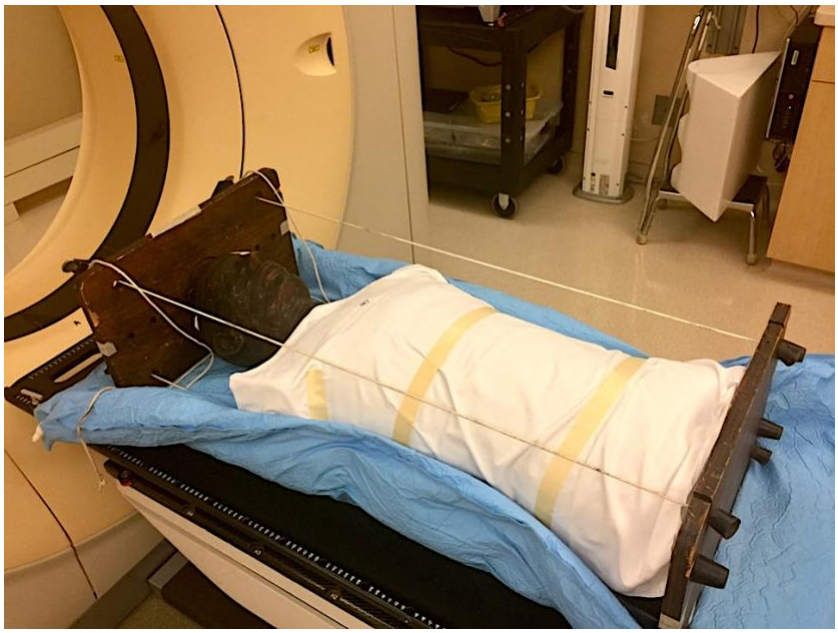

Figure 2-1. A anthropomorphic Rando phantom covered with a white sheet in order to be visible to the SIGRT cameras. The phantom was positioned on a Vac-Lok vacuum cushion.

In the treatment room, each setup was reproduced in a Varian Truebeam LINAC (Varian Medical Systems, Palo Alto, CA) room equipped with C-RAD Catalyst HD system. The

surface area of the phantom visible using each frame was assessed. In the case of Bionix Omni V frame, both the rigid plate and the respiratory belt were examined. The placement of a respiratory trace was also evaluated.

2.3. Results

Figure 2-2, Figure 2-3, Figure 2-4, and Figure 2-5 show the phantom setup on the treatment room and the surface images recorded by Catalyst.

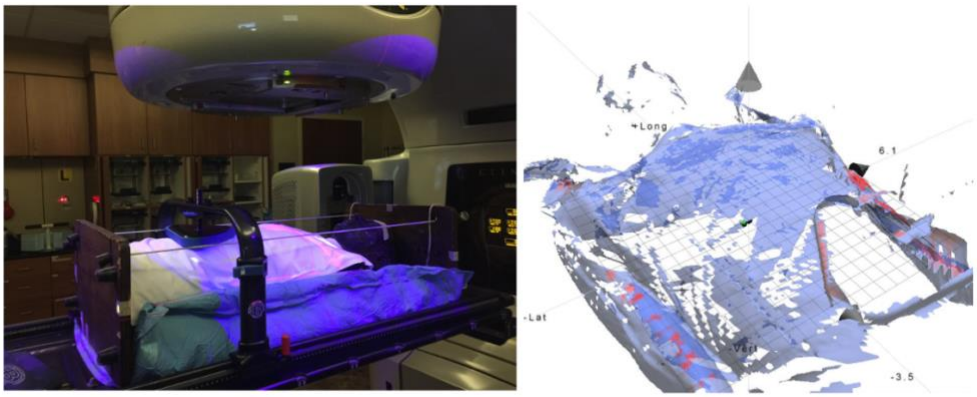

(a) (b)

Figure 2-2. Illustration of phantom setup on the treatment room using Bionix Omni V stereotactic body frame and compression plate (a), and the surface image recorded by CatalystHD (b).

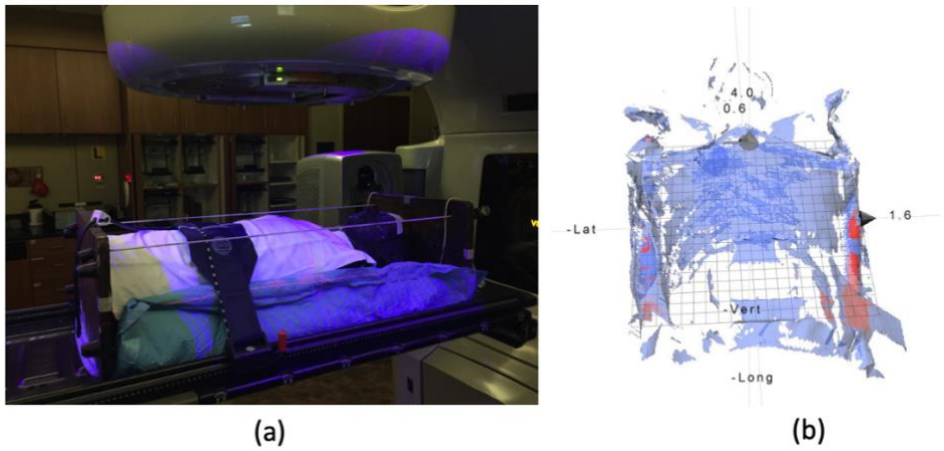

Figure 2-3. Illustration of phantom setup on the treatment room using Bionix Omni V stereotactic body frame and respiratory belt (a), and the surface image recorded by CatalystHD (b).

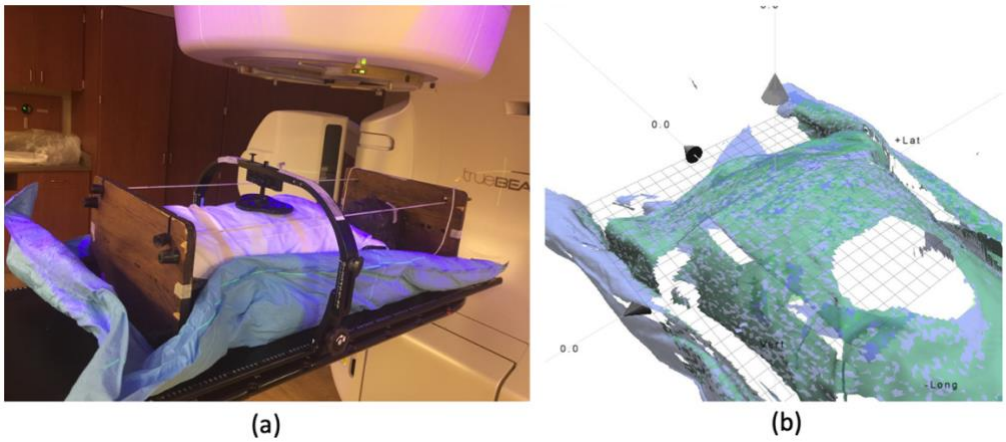

Figure 2-4. Illustration of phantom setup on the treatment room using Civco body Pro-lok stereotactic body frame and compression plate (a), and the surface image recorded by CatalystHD (b).

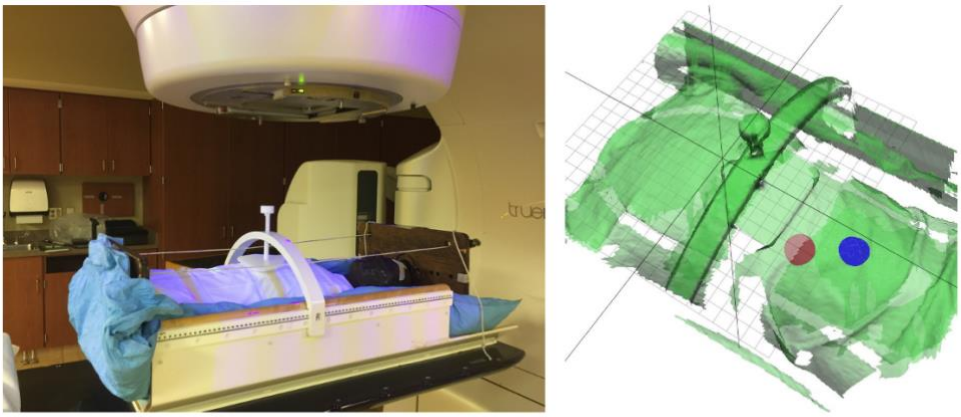

Figure 2-5. Illustration of phantom setup on the treatment room using Elekta Body Frame stereotactic body frame and compression plate (a), and the surface image recorded by CatalystHD (b).

The phantom surface area visible to the CatalystHD cameras varies depending on the immobilization frame used. The surface area in Bionix Omni V frame provides the largest visible area. Due to the variations of the colors of the frames, there are obvious differences in the amount of reflection of each frame and the degree in which they obstruct the skin rendering. Depending on the color of the SBRT frame and its contrast with the surface, the frame may be automatically excluded from the surface allowing only the phantom surface to be monitored by the CatalystHD camera. However, compression plates in all three frames are an obstacle in recording the respiratory signals.

2.4. Conclusion

SBRT frames increase the precision of patient positioning and decrease the uncertainty of target tracking by reducing the intra-fraction motions. Combining the use of CatalystHD, and volumetric imaging with SBRT positioning frames adds another level of accuracy to patient setup and provides monitoring of the movements during treatment. The utility of the surface imaging with SBRT frames, however, is limited by the obstruction of the surface image by the compression plate and the color of the frame.

Chapter 3

3.A Patient-Specific Correspondence Model to Track Tumor Location in Thorax during Radiation Therapy

3.1. Introduction

The main goal of a radiation therapy treatment plan is to deliver the maximum radiation dose to the tumor while sparing the organs at risk. A precise measure of the tumor location is crucial for achieving this goal. For many treatment sites, respiratory-induced motion makes the measurement and tracking of the exact tumor location more difficult during radiation delivery.

Different methods have been developed to locate the tumor during radiation delivery. Among these methods, real-time tumor tracking by implanted markers and fluoroscopy have been found to be very accurate [70], [71]. As bones and other high density structures block the tumor, imaging the tumor by x-ray (fluoroscopy) alone is challenging [72], [73]. Therefore, fiducial markers are often implanted into or adjacent to the tumor. However, these methods include additional risks and complications, such as extra radiation exposure to the patient and invasive fiducial marker implantation procedures. Another disadvantage

of tracking tumors by fluoroscopy and markers is the possibility of markers' migration from the implantation site [74].

In one type of gated radiation therapy, the beam is switched off when the tumor exits the target region (e.g., during inhalation) and switched on when it moves back to the target region. Although gated radiation therapy can increase the efficacy of radiation delivery despite organ and tumor motion, this method of gating increases the treatment time [75]. Also, there can be a time delay between when the beam turns on and the time of marker identification that would affect the accuracy of the treatment [38], [76].

Tracked treatments are another type of gated radiation therapy, and include robotic-arm-mounted linear accelerator (LINAC) and dynamic multi-leaf collimator (MLC) treatment deliveries. These can successfully reduce the planning target volume (PTV) margins and therefore reduce the exposure to the healthy tissue around the target as they actively modify the treatment delivery. However, imaging the tumor during radiation therapy is not always straightforward. For some lung tumors, only x-ray images from particular angles can reliably point out the location of the tumor [49], [77].

An alternative approach is to calculate the location of the tumor during treatment. This may be done by finding a correlation between internal motion (motion of the tumor) and one or more respiratory surrogate signals such as spirometry or displacement of the patient's chest or abdomen [78]–[85] This correlation is often expressed as a correspondence model and is made prior to the treatment. Figure 3-1 shows how a correspondence model is typically made.

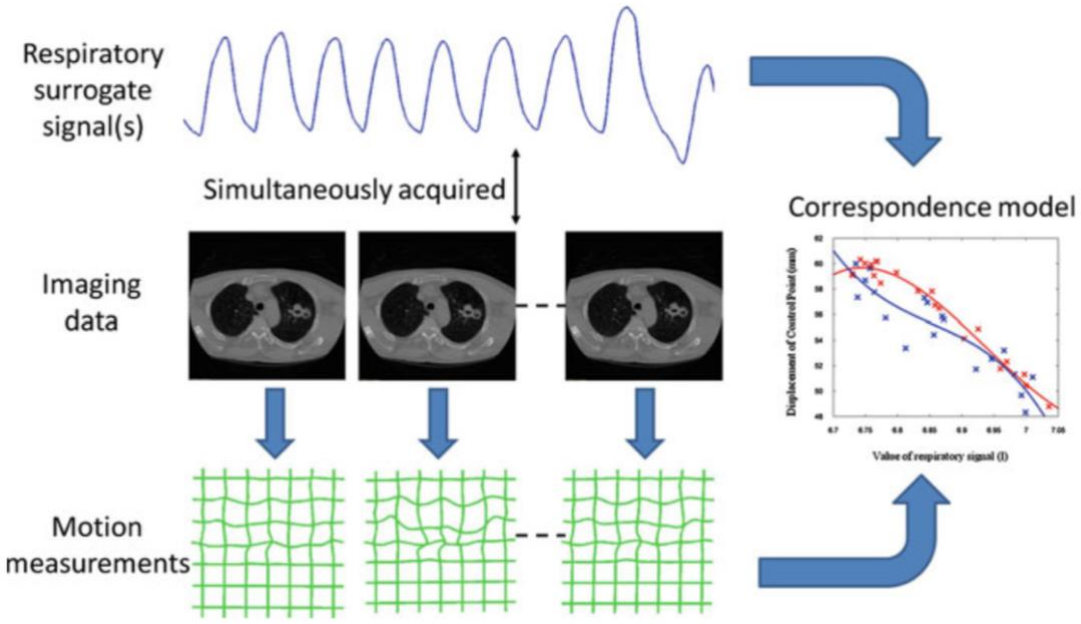

Figure 3-1. Demonstration of how a correspondence model is typically made (figure from Ehrhardt and Lorenz (Eds.), 2013[75]).

Internal motion is often measured by performing image processing techniques on images from modalities such as magnetic resonance imaging [86]–[88] (MRI), four dimensional computed tomography (4DCT) [78], [79], [89], cone-beam CT [90] (CBCT) and fluoroscopy [91], [92].

A high-quality surrogate signal is easy to measure throughout the radiation delivery, so the correspondence model gives the estimation of the tumor location [75]. There are different choices of surrogate signals. Some studies use internal surrogate signals, which are mostly derived from the patient's images, such as displacement of some points of the internal anatomy like the diaphragm [89]. Although the correlation found would be stronger compared to the use of external surrogate signals, updating these signals during radiation

delivery might be challenging due to the poor quality images. In addition, they introduce more radiation exposure to the patient. In contrast, external surrogate signals such as displacement of the patient's chest or abdomen can be measured directly. These are favorable since they are easy to measure during the course of treatment and do not include further exposure or invasive procedures.

Presented here is a method to develop a patient-specific correspondence model to calculate tumor location in the chest during radiation treatment. The proposed model is made prior to the treatment for each patient. 4DCT images of the patient are used as the knowledge of the patient's internal motion, and the displacement of two points on the patient's skin in the thoracic area are selected as surrogate signals. The two types of data are acquired simultaneously. Principal Component Analysis (PCA) [93], is used to fit the correspondence model. The model incorporates surrogate signals as input and delivers the 3D trajectory of the tumor center voxel or any other voxel of interest as output. The accuracy of the model was evaluated on a respiratory phantom and lung cancer patients.

Twenty patients with lung cancer were entered into our study. However, due to limitations and technical problems (inaccurate data acquisition, improper placement of the primary and/or secondary signal location, equipment malfunction), only the data of five patients were complete and usable for the study.

This study was approved by the University of Minnesota Institutional Review Board (IRB), and all patients provided consent to be included in the study.

The patient treatments were not gated and patients were instructed to breathe normally during both the 4DCT acquisition and treatment.

This model offers a non-invasive and dose-free technique for tumor tracking with potential to enter clinical use due to its utilization of a commercially available system. This chapter first explains the general method to develop the correspondence model. Then, it discusses the evaluation of the model on a respiratory phantom and patient data.

3.2. Materials and Methods

Figure 3-2 demonstrates the framework of the correspondence model proposed here. After acquiring the imaging data and surrogate signals simultaneously, both types of data are processed to extract the internal/tumor and external data. Principal Component Analysis (PCA) is used to construct the correspondence model. On the treatment day, the surrogate signals are recorded and placed into the correspondence model to calculate the 3D location of the center of the tumor. Details of each step are explained in the following sections.

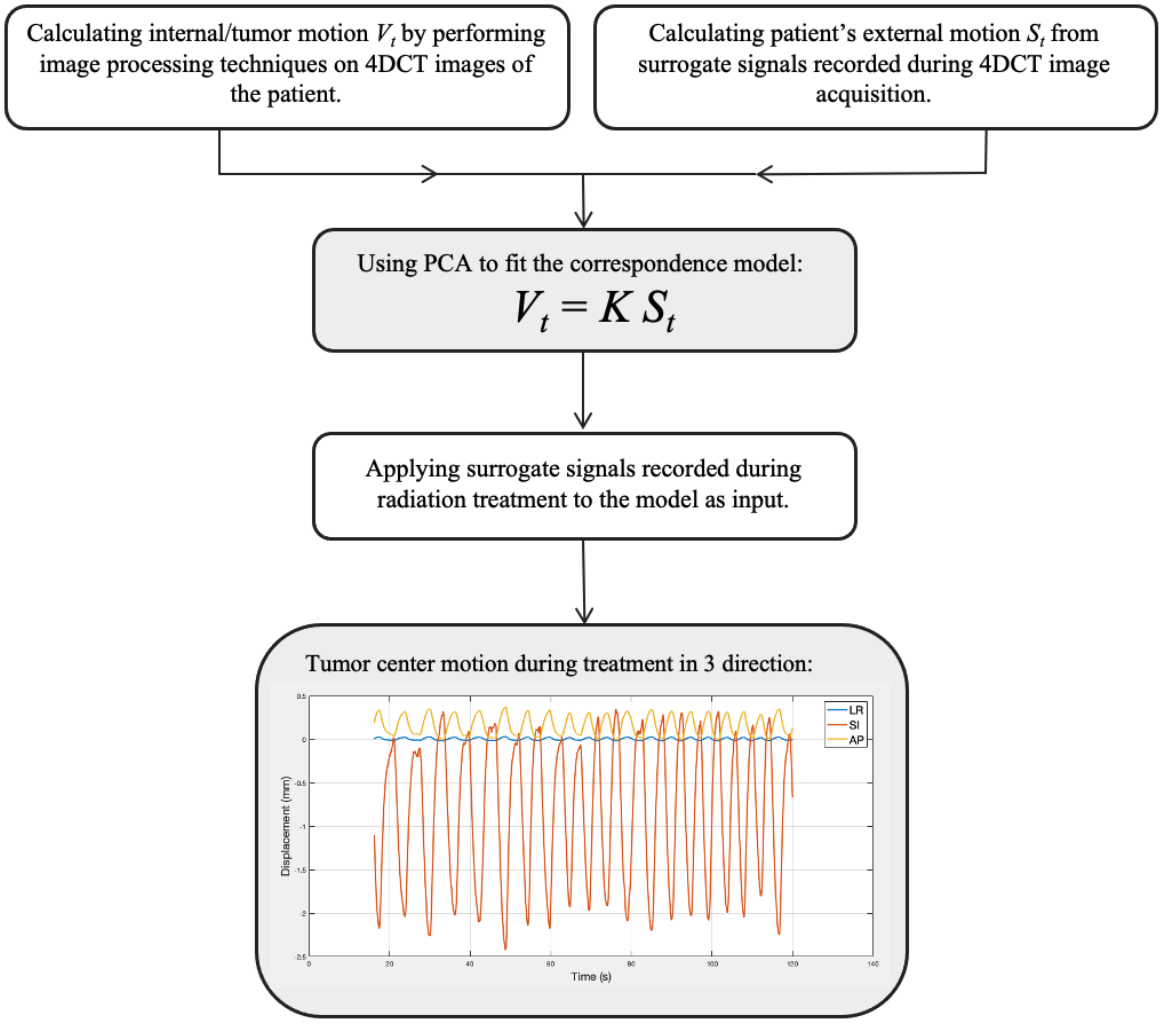

Figure 3-2. A simple representation of the framework of the proposed correspondence model. The model calculates the location of the center of the tumor in three directions, Left-Right (LR), Anterior-Posterior (AP), and Superior-Inferior (SI), during the treatment.

3.2.1. Data Acquisition for Model Construction

During CT simulation procedure, Sentinel recorded the displacements of two points on the skin surface in anterior-posterior (AP) direction as surrogate signals. The two surrogate signals were recorded as "primary signal" and "secondary signal." For all patients, the primary signal was located on the patient's skin approximately on the xiphoid process, and the secondary signal was located about 2 cm superior to the primary signal. Figure 3-3 shows the location of the primary and secondary signals on one of the patients in the study. Figure 3-4 shows the recorded primary and secondary signals for this patient. The respiratory signals were then exported from C-RAD software and imported to Matlab™ (The MathWorks Inc., Natick, MA) for processing.

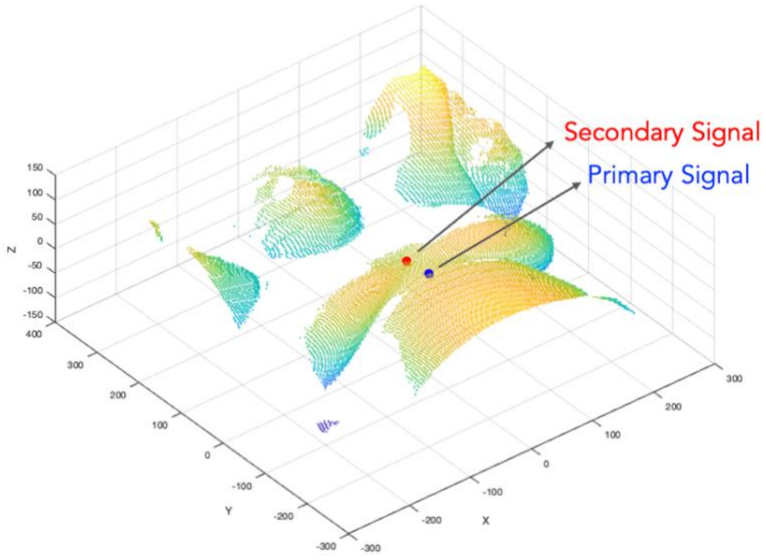

Figure 3-3. Illustration of the surface image of the patient no. 3 in the study recorded by Sentinel on the simulation day. The location of the primary and secondary signals is shown on the surface image.

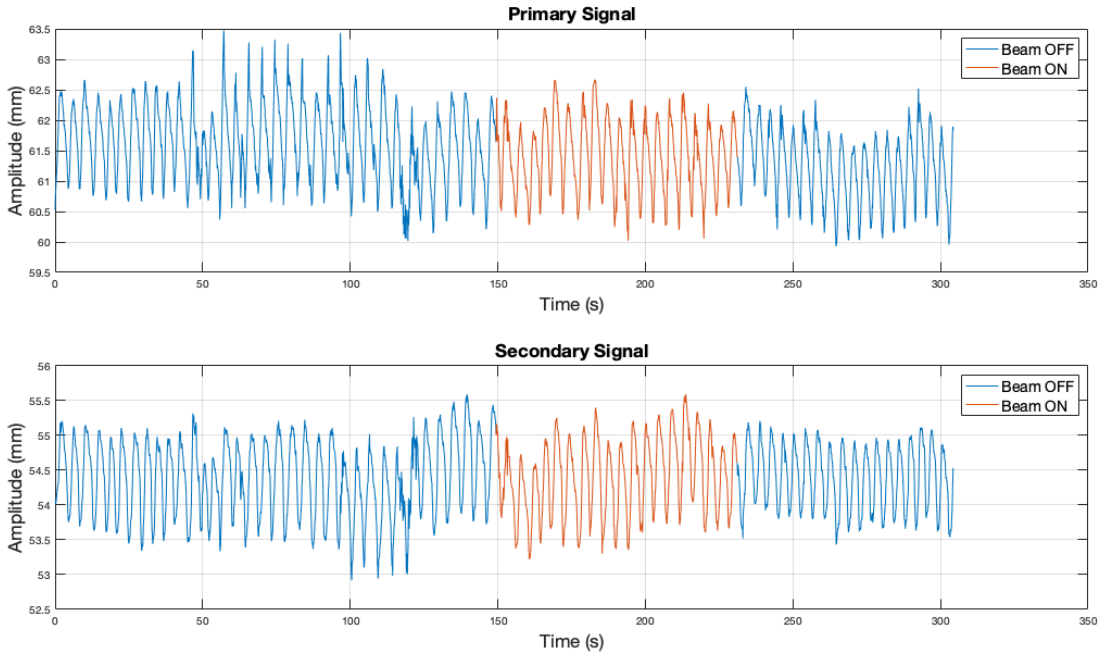

Figure 3-4. Primary and secondary signals recorded for patient no. 3 in the study. The 4DCT acquisition period is identified by red on the signals.

While recording the surrogate signals, a helical 4DCT image was acquired (120 kVp, 800 mAs/slice, FOV 600 mm) using a Philips Brilliance Big Bore CT scanner. Timestamps for the beam-on and beam-off periods of 4DCT acquisition were recorded by a stopwatch. The primary signal was used to reconstruct the 4DCT images retrospectively. The 4DCT images were sorted into ten respiratory phases (i.e., 0%, 10%, 20%, . . ., 90%) using vendor supplied amplitude-binning algorithm with the 0% as end of inhalation (EI) and 50% as end of exhalation (EE). There are two available vendor supplied binning algorithms, phase-binning algorithm, and amplitude-binning algorithm. In the phase binning algorithm, the local maxima on the respiratory signal are identified and tagged as EI. The interval between each two consecutive EI points is a complete respiratory cycle. Therefore, other respiratory

phases are identified by locating their correspondence phase value on the temporal axis. That is, 10%, 20%, . . ., 90% corresponding to phase values π/5, 2π/5, …, 9π/5 (Figure 3-5.a). In the amplitude-binning algorithm the amplitude of the respiratory signal is used for the binning process. In this algorithm after identifying all local minima and maxima on the respiratory signal, the amplitude of the EI and EE phases are calculated separately. Therefore, the amplitude-binning algorithm account for hysteresis effect and potential irregular breathing [94]. All other respiratory phases with the same amplitude are identified on the distance between EI and EE phases (Figure 3-5.b).

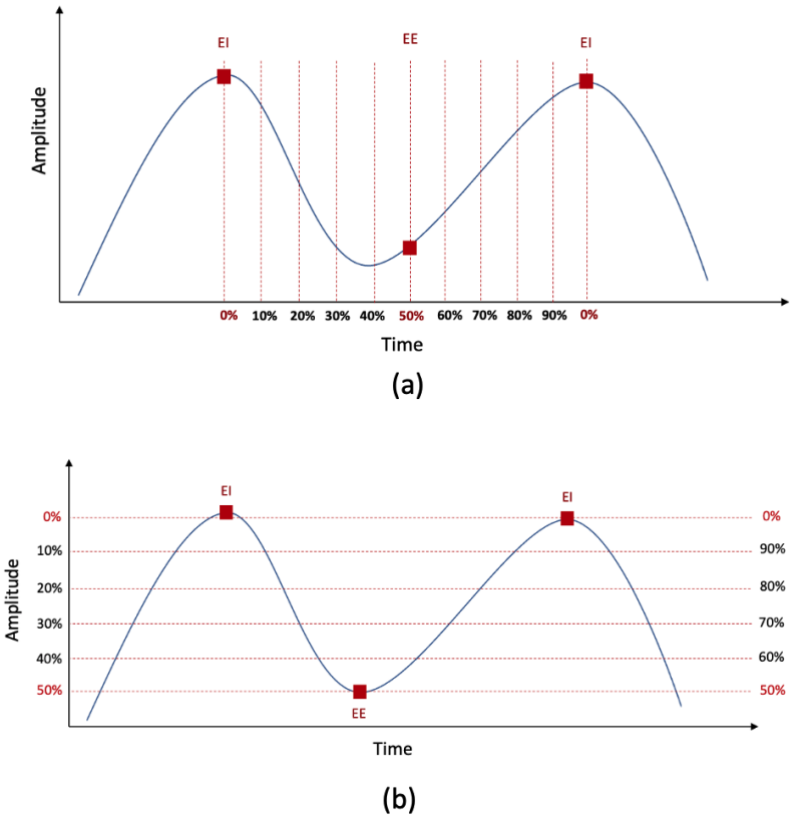

Figure 3-5. Illustration of phase-binning algorithm (a) and amplitude-binning algorithm (b) on the respiratory signal.

After 4DCT reconstruction, the image in each respiratory phase is 512×512 pixels $\times n$ slices with voxel size $1.17188 \times 1.17188 \times 3\ mm^3$. 4DCT images were exported from the CT scanner in DICOM format for further processing.

3.2.2. Surrogate signal Processing

The aim of processing the surrogate signals was to find the average displacement (amplitude) of the patient's skin surface at each respiratory phase at the location of primary and secondary signals. In other words, after processing the surrogate signals, the surrogate signal vector $S_i = [s_{1,i}, s_{2,i}]^T$ was constructed at each time point i, where $s_{1,i}$ and $s_{2,i}$ are the average amplitude of the patient's skin surface at primary and secondary signal locations, respectively at timepoint i ($i = 1,2,\dots,10$, for 10 respiratory phases).

Multiple pre-processing steps were applied to the signals. To remove the low-frequency components of the signals and to eliminate the baseline drifts, a high-pass filter was applied. Next, a Savitzky-Golay smoothing filter was applied to remove noise and smooth the signals. Using the beam ON and OFF timestamps, the period of the signals in which the beam was ON (4DCT acquisition period) was extracted to calculate the magnitude of displacement at each respiratory phase (Figure 3-6).

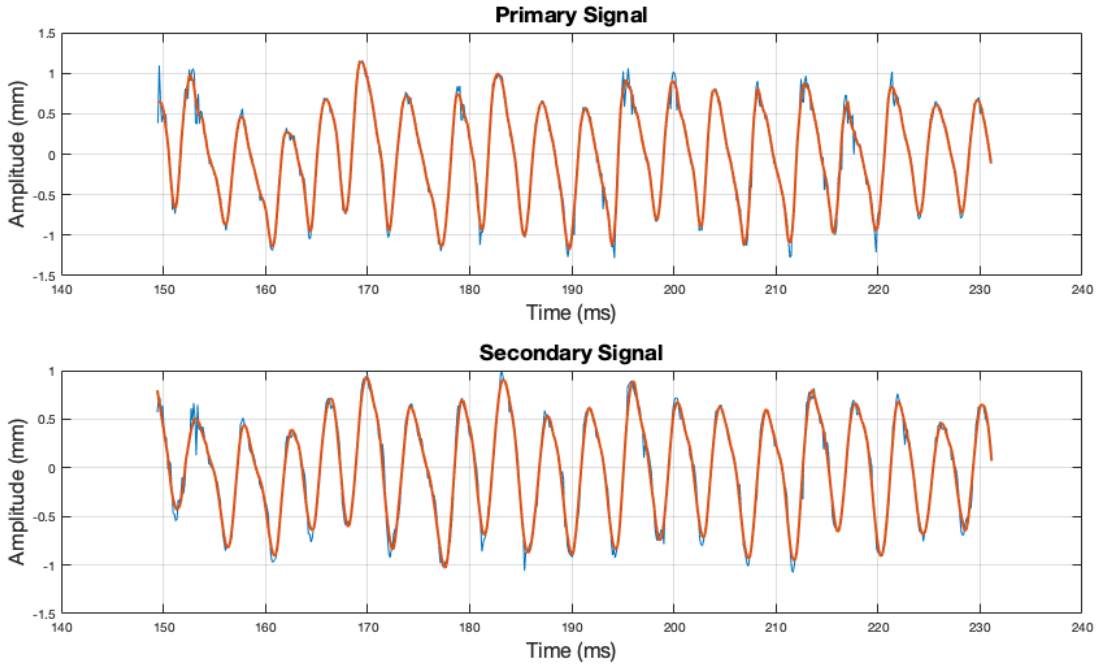

Figure 3-6. 4DCT period of the primary and secondary signals for patient no. 3 in the study. The original signals is shown in blue and the signals after pre-processing step is shown in red.

To find the average amplitude of skin surface at each respiratory phase, the amplitude binning algorithm was chosen. First, for each signal, on the trace of amplitude vs. time, all the minima and maxima were located. Then the average amplitude of all minima and the average amplitude of all maxima were calculated and set as extremities (Figure 3-7). Therefore, to compute the average amplitude of 0% and 50% phases, the amplitude of any maximum or minimum that exceeded these limits was replaced by the magnitude of the average amplitude of the maxima or minima. This process would exclude any shallow or deep breaths of the patient.

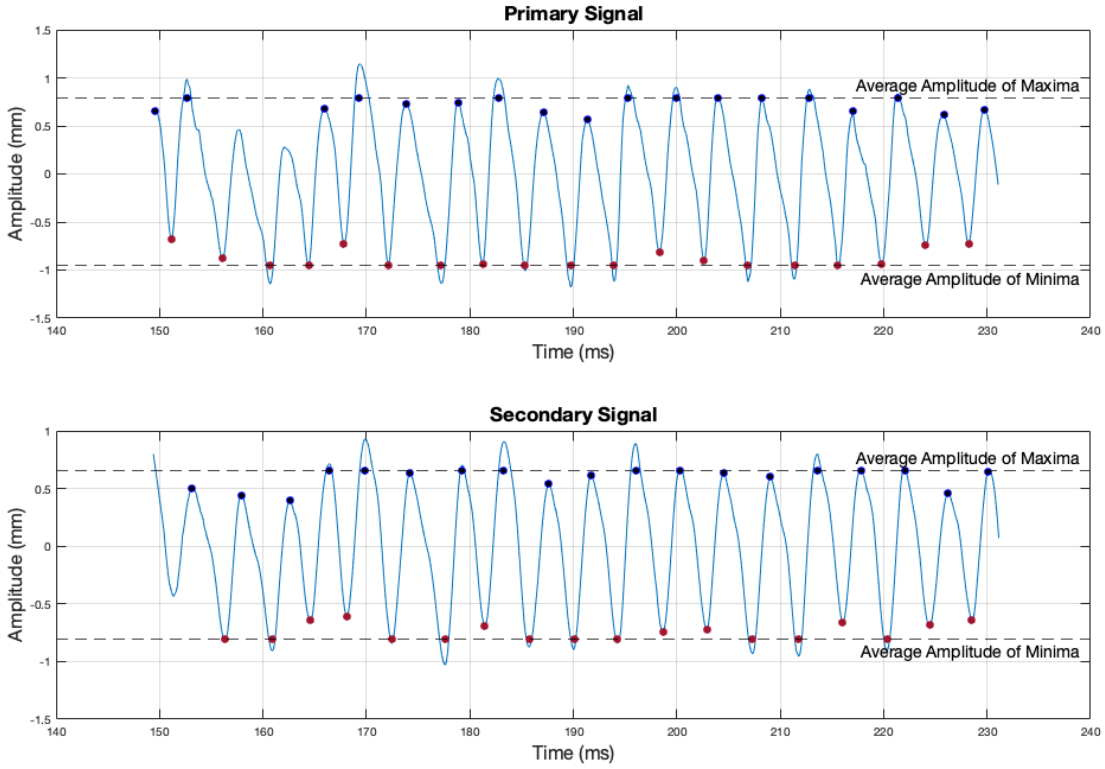

Figure 3-7. For calculation of average amplitude of each respiratory phase, after identifying all the minima and maxima on each signal, the average amplitude of maxima and the average amplitude of all minima were calculated and set as extremities (signals in the image from patient no. 3 in the study).

To calculate the amplitude of the remaining respiratory phases, four points at equal distances divided the interval between the calculated 50% and 0% average amplitudes. The first point specified the amplitude of the 40% and 60% phases, the second point specified the amplitude of the 30% and 70% phases, the third point specified the amplitude of the 20% and 80% phases, and finally, the fourth point specified the amplitude of the 10% and 90% phases (Figure 3-8).

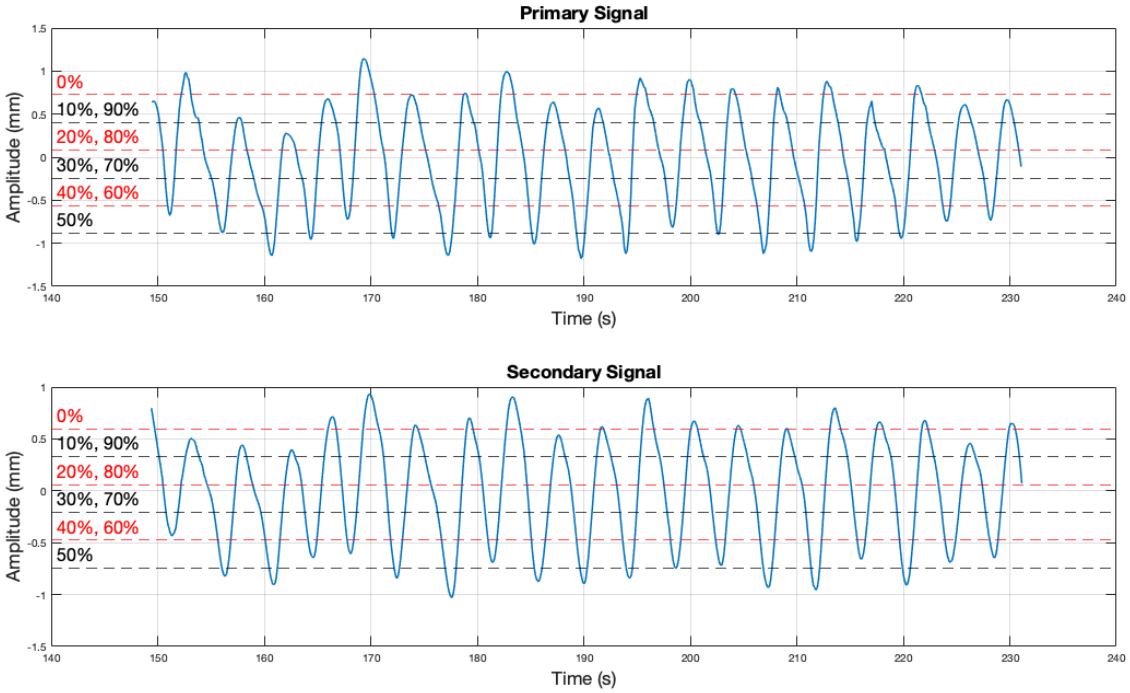

Figure 3-8. After calculation of the amplitude of EI (0%) and EE (50%) phases, to calculate the amplitude of the remaining respiratory phases, four points at equal distances divided the interval between the calculated 0% and 50% average amplitudes (signals in the image from patient no. 3 in the study).

To set the amplitude of displacement at 50% phase (EE) at zero (reference), the magnitude of average amplitude at 50% phase was subtracted from all respiratory phases. Figure 3-9 illustrates the average amplitude of ten respiratory phases calculated for patient no. 3 in the study.

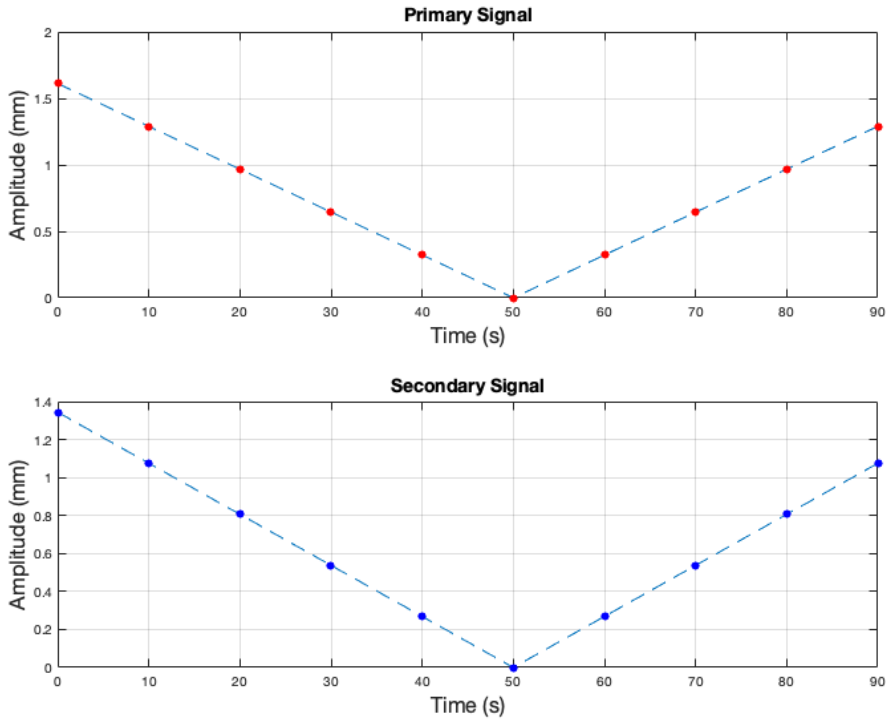

Figure 3-9. Illustration of calculated average amplitude of each respiratory phase for patient no. 3 in the study.

3.2.3. 4DCT Image Processing

Image registration can provide useful information on the displacement of the anatomical elements from one respiratory phase to the other. For most organs in the body, such as lung, large number of degree of freedom (DOF) is required to explain the deformations with required accuracy. Deformable (non-rigid) registration can describe the deformation by a large number of free parameters, contrary to affine (rigid) registration, which can work only with a limited number of free parameters [95].

In this study, deformable image registration (DIR) was performed between a reference respiratory phase and other phases. The EE phase was considered as the reference phase. The better reproducibility of the EE phase was the reason for this selection. The Horn and Schunk optical flow registration algorithm [96] was chosen for its accuracy and computational efficiency [97]. Optical flow algorithms represent the pattern of movement velocities of intensities in an image. Therefore, they work with the relative velocities of the objects in an image to an observer. If I_m and I_f represent the moving image and the fixed image respectively, the deformation vector field V is registering I_m to I_f :

$$I_f = I_m \circ V \equiv I_m\big(x - V(x)\big) \tag{2.1}$$

where, $\circ$ is composition operator and x is the spatial coordination. The above equation can be solved by adding the regularization constraint function, R. The system cost function E is:

$$E = \int_\Omega \Big(\big(I_f - I \circ V\big)^2 + \alpha^2 R(V)\Big)\, d\Omega \tag{2.2}$$

In most optical flow algorithms $R(V) = tr((\nabla V)^T(\nabla V))$, where $tr(\,)$ is matrix trace operator. In cases that $|V|$ is small, Tylor expansion of the first order term of the above equation is used:

$$E = \int_\Omega \big((I_d + \nabla I \cdot V)^2 + \alpha^2 R(V)\big) d\Omega \tag{2.3}$$

where, $I_d = I_f - I_m$, ∇ is the gradient operator and $\cdot$ is the inner vector product. In Horn and Schunk optical flow algorithm the following iterative solution is used to solve the cost function equation:

$$V_{n+1} = \bar{V}_n - \frac{(I_d + \bar{V}_n \cdot \nabla I)\nabla I}{\alpha^2 + |V|^2} \tag{2.4}$$

where, V_n is the deformation vector field (DVF) at iteration n and $\bar{V}_n$ for each pixel is averaged over neighboring pixels. Each DVF demonstrates the displacement of a voxel from the reference respiratory phase to another.

DIRART [98] software package was used to perform image registration. Nine image registration were performed between the reference phase and nine other respiratory phases. To perform each registration, in DIRART, after loading the images, a priori alignment of fixed and moving images was performed by the center of objects in both images. In order to increase the accuracy of the registration and to save the small features in the image, downsampling was performed by a multigrid approach with a maxfilter [97]. Then, the Horn and Schunk optical flow was selected as the registration algorithm. The result of DIR between the reference image (EE) and the image at time point i is a set of DVFs. Figure 3-10 represents a schematic view of the resultant DVFs after registering EI (or 0%) phase with EE (or 50%) phase on coronal view for one of the patients in the study.

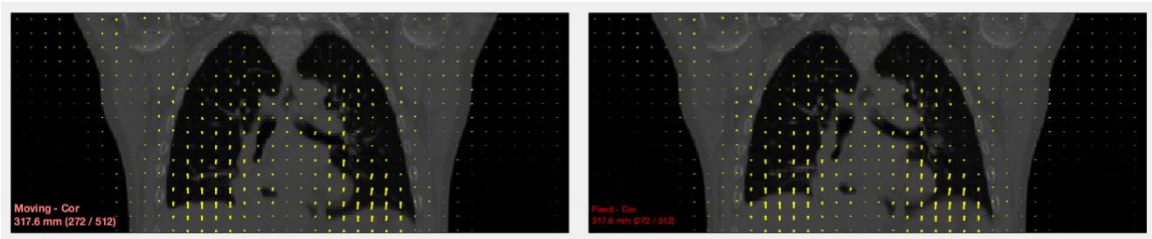

Figure 3-10. Illustration of a schematic view of DVFs resulting from registration of EI (or 0%) and EE (or 50%) phases on the coronal view of one of patient no. 4 in the study. The image on the left is the moving image (EI) and the image on the right is the fixed image (EE).

The resultant nine DVF sets were exported from DIRART to Matlab workspace for further steps of the study. Each DVF set is imported into Matlab workspace as a 3D matrix with the size of the registered 4DCT images, i.e., $512 \times 512 \times n$. Where, n is the number of slices in the image. In order to increase the speed of the computation, the majority of the DVFs of the voxels that did not include the lung were removed prior to the next steps of the study by the following steps. Since the 0% respiratory phase (EI) is the phase with lungs at their maximum size compare to other phases, first, the whole lung was segmented from EI phase. An active contour method was chosen to segment the lung. Initial seed mask was created by segmenting the lung in two perpendicular slices; one slice in XY direction (transverse) and one slice in XZ direction (coronal). Segmentation of two slices was performed by the threshold method and morphological operators. The two segmented slices are then used to make a 3D seed mask. Finally, the lung in the 3D volume is segmented by active contour method. After segmentation the value of all pixels that do not contain lung will be zero. By identifying the indices of all voxels with non-zero value, a cuboid volume was found that contains the whole lungs in 0% respiratory phase. Then, 20 voxels were added to the cuboid in each direction to make sure that all of the necessary DVFs are included in the selected matrix. Finally, in the DVF matrix, all of the voxels with the same indices as the cuboid were selected as a new DVF matrix.

The computed DVFs in DIRART are in unit of voxel (not in physical unit like cm or mm). Therefore, they were scaled by the size of the voxels in the image which is $1.17188 \times 1.17188 \times 3$. After performing some simple matrix operations the vector of

deformation fields at time point i was written as $V_i = \left[\vec{v}_{1,i}, \vec{v}_{2,i}, \dots, \vec{v}_{M,i}\right]^T$, where M is the number of voxels in the image.

3.2.4. Constructing the Correspondence Model

Principal Component Analysis is a mathematical technique for finding the pattern of data. Also, PCA can reduce the number of variables in a high dimensional dataset to a smaller number of linearly uncorrelated variables named principal components while keeping the important information.

To find the correlation between the internal motion and surrogate signals, PCA was used to fit the correspondence model [89]. PCA also has the advantage of removing the noise of the imaging data and co-linearity of surrogate data.

In PCA framework, the covariance matrix was constructed and its eigenvectors were obtained. Those eigenvectors with the largest eigenvalues are the principal components used in the model. To construct the data covariance matrix, first, motion vectors at each time point i were constructed by combining the deformation field vector and surrogate signal vector, $p_i = [V_i, S_i]$. The motion vectors have been rewritten as $p_i = \left[v_{1,1,i}, v_{1,2,i}, v_{1,3,i}, \dots v_{m,j,i}, \dots, v_{M,3,i}, s_{1,i}, s_{2,i}\right]^T$. Where, $v_{m,j,i}$ is the jth ($j = 1 - 3$ for x, y and z) displacement components of voxel m at time point i ($i = 1 - 10$, for 10 respiratory phases).

After calculation of mean motion vector ($\bar{p} = \frac{1}{10}\sum_{i=1}^{10} p_i$), matrix $P = [\tilde{p}_1, \tilde{p}_2, \dots, \tilde{p}_i, \dots, \tilde{p}_{10}]$ was constructed, where $\tilde{p}_i = p_i - \bar{p}$ is the mean centered motion vector at i. The goal was to find the eigenvectors of the covariance matrix PP^T. The size

of the P is $(3M + 2) \times 10$ and in our study M is around 10^7. Therefore, the size of the covariance matrix is large and calculating its eigenvectors is computationally expensive. However, since the total number of time points is smaller than the number of voxels in each image ($10 < M$), PP^T has only $10 - 1 = 9$ eigenvectors with non-zero eigenvalues.[31] Consider that A is the eigenvector of the $P^T P$ with eigenvalue of α ($P^T PA = \alpha A$). By multiplying both sides by P we have $PP^T PA = \alpha PA$. This shows that $E = PA$ is an eigenvector of PP^T. Therefore, instead of calculating the eigenvectors of PP^T, we can calculate the eigenvectors of the matrix $P^T P$ which is a much smaller matrix (10×10) and multiply them by P. The mean centered motion vector at an arbitrary time t is a weighted linear combination of the first G eigenvectors with the largest eigenvalues (principal components), as shown in equation 1:

$$\tilde{p}_t \approx \sum_{g=1}^{G} w_g E_g \tag{2.5}$$

Equation 2.5 can be re-written as equation 2.6:

$$\tilde{p}_t \approx EW \tag{2.6}$$

where, E is the matrix of the first G eigenvectors and W is the matrix of their related weights. Equation 2.6 can be split into two individual equations (2.7 and 2.8):

$$\tilde{v} \approx E_u W \tag{2.7}$$

$$\tilde{s} \approx E_S W \tag{2.8}$$

where, E_u and E_S are built from the upper $3M$ rows and lower 2 rows of matrix E, respectively. W can be eliminated from above equations if the inverse matrix E_s^{-1} exists:

$$\tilde{v}_t \approx E_s \, E_s^{-1} \tilde{s}_t \tag{2.9}$$

E_s^{-1} exists if the number of rows in E_s would be equal to or larger than the number of columns. In other words, the number of eigenvectors that are used in equation 1 should not exceed the number of surrogate signals.

The motion vector at time t can be calculated from new surrogate signal values by equation 2.10:

$$V_t = \bar{V}_i + E_s E_s^{-1}(S_{new} - \bar{S}_i) \quad (2.10)$$

where, $\bar{S}_i = \frac{1}{10}\sum_{i=1}^{10} S_i$ and $\bar{V}_i = \frac{1}{10}\sum_{i=1}^{10} V_i$. The components of the vector $S_{new} = [s_{1,t}, s_{2,t}]^T$ are the new values of the surrogate signals, i.e. the inputs of the correspondence model.

3.2.5. Surrogate Signals as the Model Input

During treatment, CatalystHD recorded the primary and secondary signals. The location of the primary and secondary signals on the patient's skin on treatment day are the same as their location on the CT simulation day. After the treatment the signals were exported from the C-RAD software and imported to Matlab. Figure 3-11 illustrates the primary and secondary signals recorded by CatalystHD for one of the patients in the study.

The average amplitude of 50% respiratory phase (EE) was calculated for both primary and secondary signals (with the same method that was explained before) and was set as the baseline (zero). Then, the primary and secondary signals were entered into the correspondence model as input.

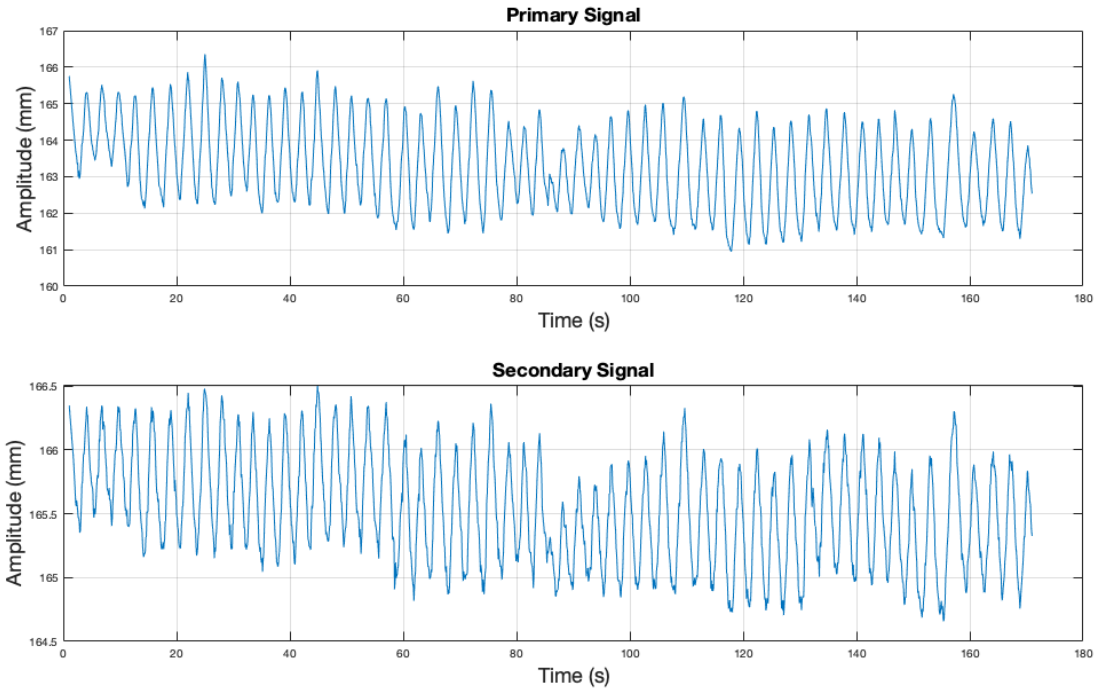

Figure 3-11. Illustration of primary and secondary signals recorded on the treatment day for patients no. 3 in the study.

3.2.6. Respiratory Phantom

To evaluate the accuracy of the correspondence model, the model was tested on a respiratory phantom. A CIRS Xsight Lung Tracking Phantom kit (CIRS, Norfolk, VA) was used to model the respiratory motion (Figure 3-12).

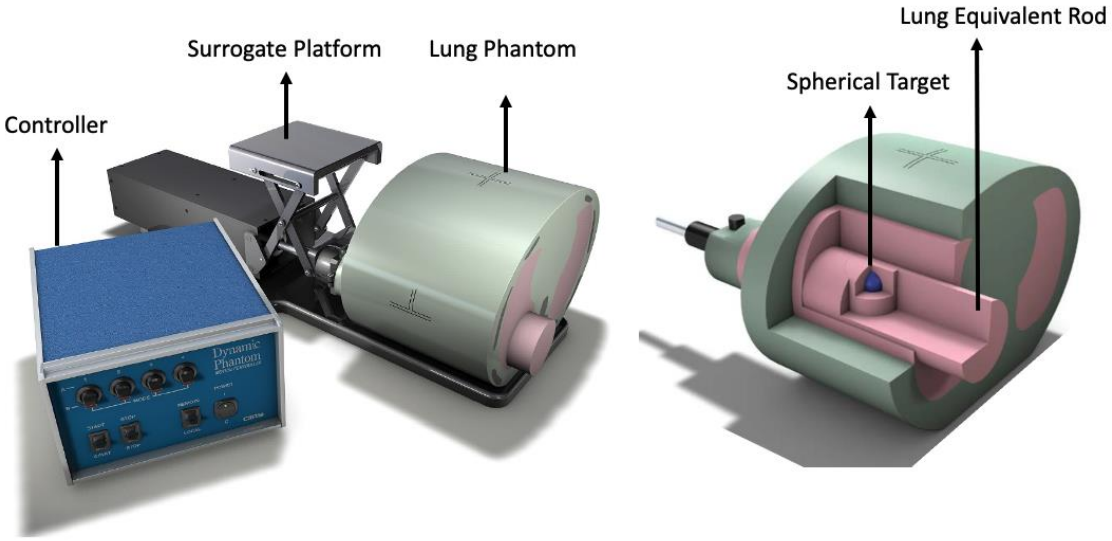

Figure 3-12. CIRS Xsight Lung Tracking Phantom kit.

A 25 mm diameter spherical target is embedded inside a 63.5 mm diameter lung density-equivalent rod. As the surrogate platform moves vertically, the rod moves 10 mm linearly, and rotates with a rotational amplitude of 10.3 degrees in the phantom. A complete cycle is defined as an EE followed by an EI. Each complete cycle takes 4.5 s. The center of the sphere moves 10 mm in superior-inferior (SI) direction, 0.24 mm in anterior-posterior (AP) direction, and 2.77 mm in left-right (LR) direction. These values were considered as ground truth for the phantom study.

A thin wooden board, approximately 1 mm thick, was attached to the top of the phantom platform to expand its area. A large skin-like silicone pad was placed on the phantom to simulate skin and, to cover the board on the surrogate platform and connect it to the phantom. The primary signal point was placed on the surrogate platform, and the secondary

signal was placed on the part connecting the platform to the phantom. The isocenter was considered at the target sphere centroid.

The phantom 4DCT and surrogate signals were acquired, and the correspondence model was constructed for the phantom. Figure 3-13 illustrates the setting of the phantom on the CT scanner's couch.

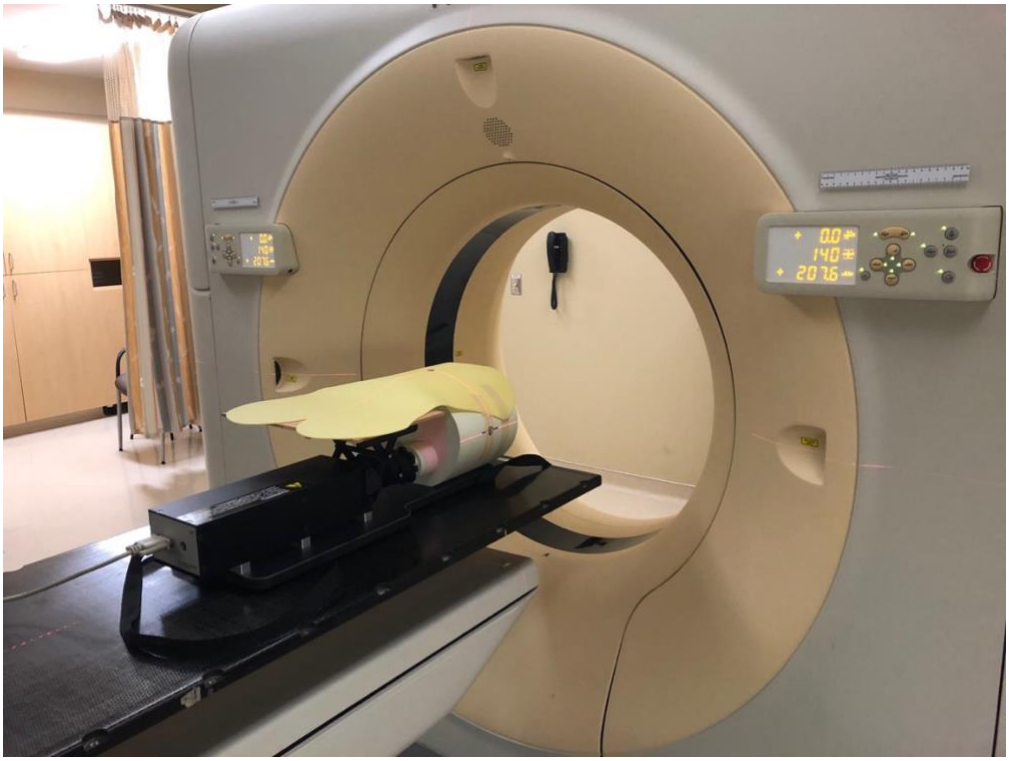

Figure 3-13. A CIRS Xsight Lung Tracking Phantom as positioned on the CT scanner couch. A large skin-like silicone pad was placed on the phantom to cover the surrogate platform and connect it to the phantom.

The phantom was then positioned on the treatment couch of a Varian Truebeam LINAC (Varian Medical Systems, Palo Alto, CA). Figure 3-14 shows the setup of the phantom on the linear accelerator couch. The primary and secondary signals were recorded by CatalystHD and were placed into the model to calculate the target sphere centroid's motion in SI, AP and LR directions. The average and standard deviation of displacement between all consecutive EE and EI phases were calculated and compared with the ground truth.

Figure 3-14. A CIRS Xsight Lung Tracking Phantom as positioned on the linear accelerator couch. A large skin-like silicone pad was placed on the phantom to cover the surrogate platform and connect it to the phantom. The red and light green circles on the silicon pad represent the position of primary and secondary signals, respectively.

3.2.7. Patient Data

After recording the surrogate signals and 4DCT images of each patient on the simulation day, the correspondence model was constructed. The surrogate signals were also recorded by CatalystHD during each treatment session and entered into the model to calculate the location of the voxel of interest during treatment. Table 3-1 shows the characteristics of the patients in the study. The last two columns of Table 3-1 shows patients' breathing types. Periodic combination of shallow and deep breathing patterns was considered irregular breathing and uniform respiration was considered regular breathing.

Table 3-1. Characteristics of the patients in the study.

Patient no.	**Sex**	**Age**	**Tumor Location**	**Breathing type Simulation Day**	**Breathing type Treatment Day**
1	F	77	Upper right lung	Irregular	Irregular
2	M	70	Upper right lung	Regular	Regular
3	F	59	Lower left lung	Regular	Regular
4	M	62	Lower right lung	Irregular	Regular
5	M	50	Lower right lung	Regular	Regular

Two of the patients (patients 1 and 2) had tumors that were visible in approximately half of the 2D projections. Therefore, it was possible to calculate the tumor range of motion from 2D projections as ground truth for the model. For those patients, the motion trace of the tumor center was calculated by the model in the SI, AP, and LR directions. In the

resultant trace of displacement vs. time in each direction, the magnitude of displacement of the tumor center between any two consecutive EE and EI phases, and their average and standard deviation, were calculated. The tumors of the other three patients (patients 3, 4, and 5) were not visible in the 2D projections, due to their proximity to other structures such as diaphragm. Therefore, the motion trace of the apex of the diaphragm on the ipsilateral side of the tumor was calculated by the model in the same three directions. In the resultant trace of displacement vs. time in each direction, the magnitude of displacement of the diaphragm apex between any two consecutive EE and EI phases, and their average and standard deviation, were calculated.

At each treatment session, just prior to the treatment delivery, a cone-beam CT (CBCT) image was acquired using the Varian LINAC's CBCT system. All CBCT images were acquired using "thorax" protocol (1 min, 15 frames/s, 360^{o}) in half-fan mode at 125 kV and 15 mA. During each CBCT acquisition, 895 two-dimensional (2D) projections were acquired. The 2D projections were used to calculate the ground truth on the day of treatment. To calculate the ground truth from 2D CBCT projections, first, the EE and EI projections were identified. To find the EE and EI projections, the patient's respiratory signal for the CBCT period was extracted using Amsterdam Shroud (AS) Image [99].

In this technique, the position of the diaphragm is used to extract the patients respiratory signal. First, the logarithm of each individual projection is applied. Now the value of each pixel in the image is proportional to the radiological thickness. To distinguish patient from air a threshold is applied to the logarithmic image (Figure 3-15).

In the next step, to intensify the diaphragm, the derivative of the image is taken in the SI direction using a Sobel gradient operator. In Sobel gradient operator, the pixel's gradient is a weighted sum of pixels in a 3×3 pixel neighborhood (Figure 3-16).

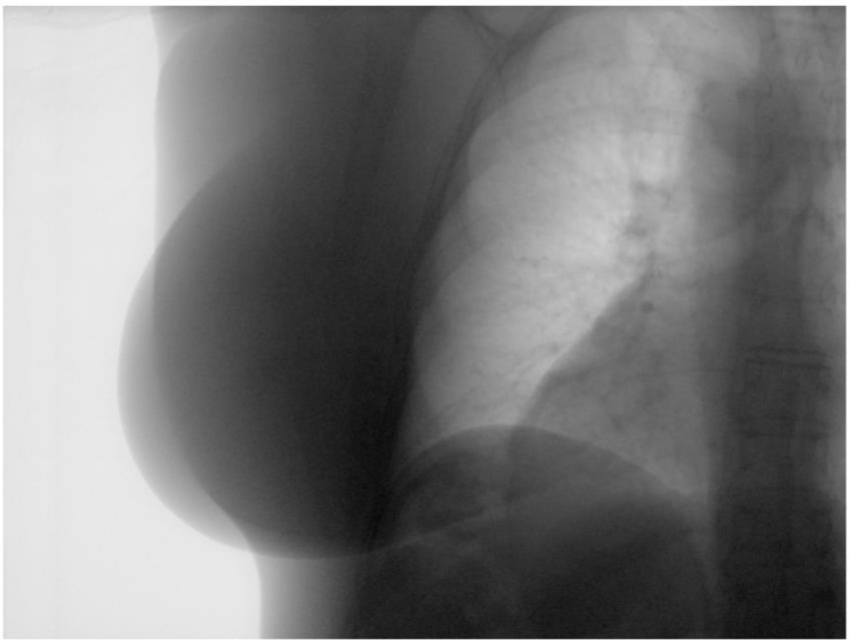

Figure 3-15. The logarithmic 2D projection of one of patient no.3 in the study in EE phase after applying a threshold.

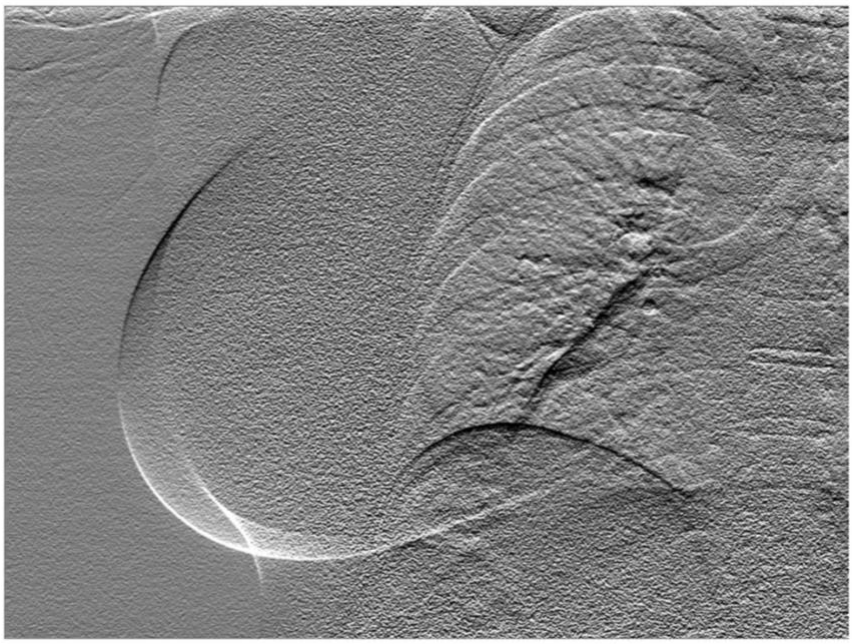

Figure 3-16. The derivative of the image in Figure 3-15 is taken in the SI direction using a Sobel gradient operator.

A threshold is applied to the derivative image to separate the diaphragm-like transitions (Figure 3-17, left). Then, the resultant image is collapsed onto its craniocaudal (SI) axis by summing over all pixel intensity values in each row to form a 1D projection (Figure 3-17, right).

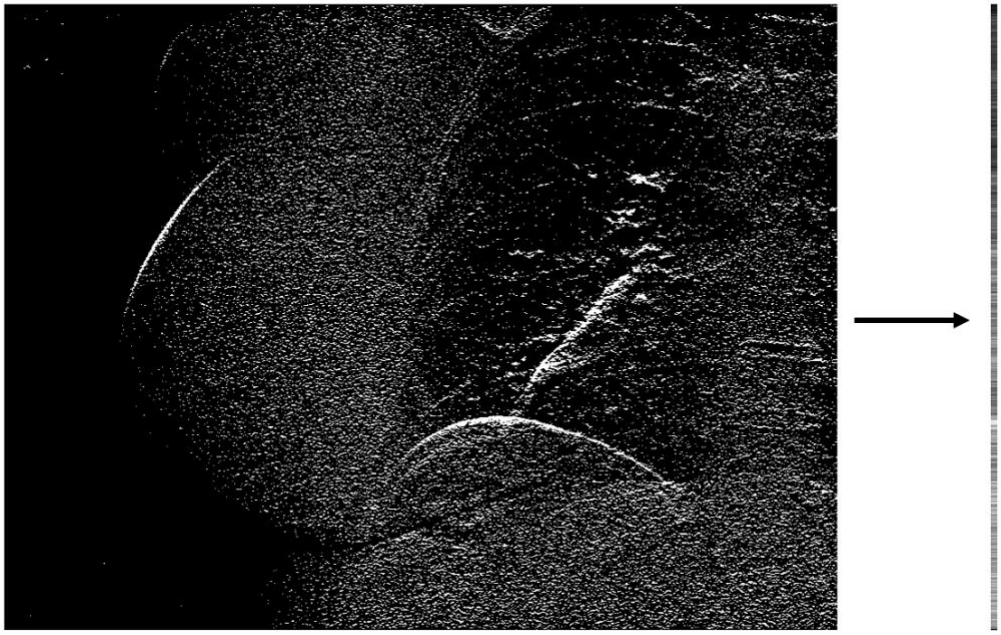

Figure 3-17. Applying a threshold to the image in Figure 3-16 (left) and it projection on craniocaudal axis at the (right).

The AS image is constructed by combining all 1D projections view by view. A horizontal derivative is applied on the AS image to highlight the diaphragm (Figure 3-18).

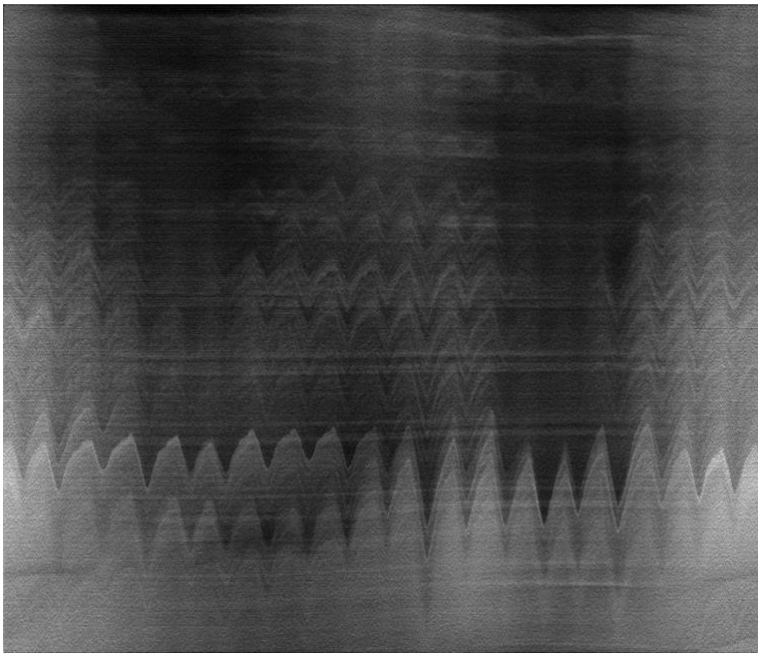

Figure 3-18. The Amsterdam Shroud image constructed for one of the patients in the study.

After cutting the diaphragm region out of the AS image (Figure 3-19.a), diaphragm region is collapsed onto the temporal (horizontal) axis by summing over all pixel intensity values in each column (Figure 3-19.b) [100]. This resultant signal has two components. One component is mostly due to respiration and the other component is due to other factors such as traversing the x-ray beam through varying thickness materials as the gantry is rotating around the patient. After applying a high-pass filter the respiratory signal is extracted (Figure 3-19.c). On the respiratory signal extracted from diaphragm motion, the projections that are on the maxima of the signal are EE phases and those on the minima of the signal are EI phase.

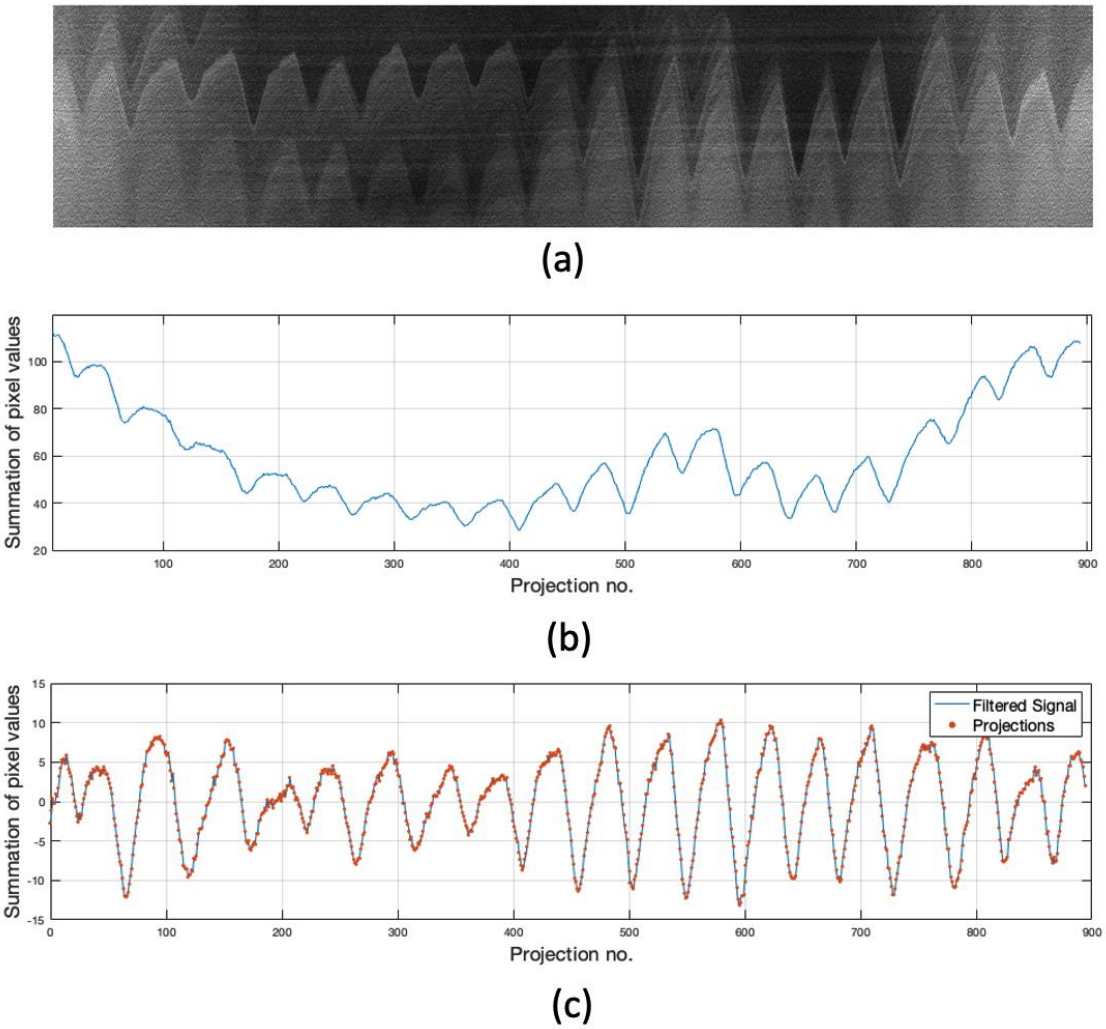

Figure 3-19. Diaphragm region was cut from the AS image (a). Diaphragm region is collapsed onto the temporal (horizontal) axis by summing over all pixel intensity values in each column (b). The respiratory signal is obtained after applying a high-pass filter. Each red point on the signal is representing a projection (c).

For patients 1 and 2, whose tumors were visible in a sufficient number of projections, a radiation oncologist drew the contour of the tumor on the 2D projection images (Appendix A). Then the centroid position of the tumor was localized in those images [101]. The

displacement of the centroid in projection images could be measured in two directions: the axial direction, which is along the SI axis of the imager, and the tangential direction, which is perpendicular to the axial direction. Since for these two patients, the CBCT center of rotation is at the tumor center, the displacement of the centroid of the tumor in the axial direction is a scaled version of the displacement in the SI direction. The displacement in the tangential direction is a combination of displacements in the AP and LR directions. However, for projection angles close to LR or right-left (RL), the displacement of the centroid is approximately a scaled version of its AP displacement, and for projection angles close to AP or posterior-anterior (PA), the centroid's displacement is approximately a scaled version of its LR displacement. The position of the centroid was calculated in all EE and EI projections for which the tumor was visible to the radiation oncologist. The difference of centroid position in the axial direction between any two consecutive EE and EI was measured, and their average and standard deviation were calculated. For AP and LR directions, the closest consecutive EE and EI projections to LR/RL and AP/PA were identified and the differences of centroid position in tangential direction were calculated.

For patients 3, 4, and 5 (for whom the displacement of their apex of the diaphragm was calculated by the model), the apex of the diaphragm was located manually on all EE and EI projections. After scaling and applying the fan-beam geometry, the average and standard deviation of the apex of the diaphragm were calculated as ground truth in SI direction. In addition, the projections near LR/RL and AP/PA were identified, and the displacement of the apex in the tangential direction was calculated as ground truth in AP and LR directions.

3.3. Results

3.3.1. Respiratory Phantom

Figure 3-20 shows the location of the target sphere centroid calculated by the model for the respiratory phantom in the LR, AP, and SI directions. The direction of the motion matches the true direction of the centroid motion along all three axes. The magnitude of the average and standard deviation of the displacement in each direction is compared with the ground truth data in Table 3-2. The error is less than 1 mm in the LR and AP directions, and less than 2 mm in the SI direction. The main component of this error is the deformable image registration accuracy. Figure 3-21.a shows the PCA eigenvalue spectrum for the respiratory phantom. To fit the correspondence model, only the eigenvector associated with the first (largest) eigenvalue was used.

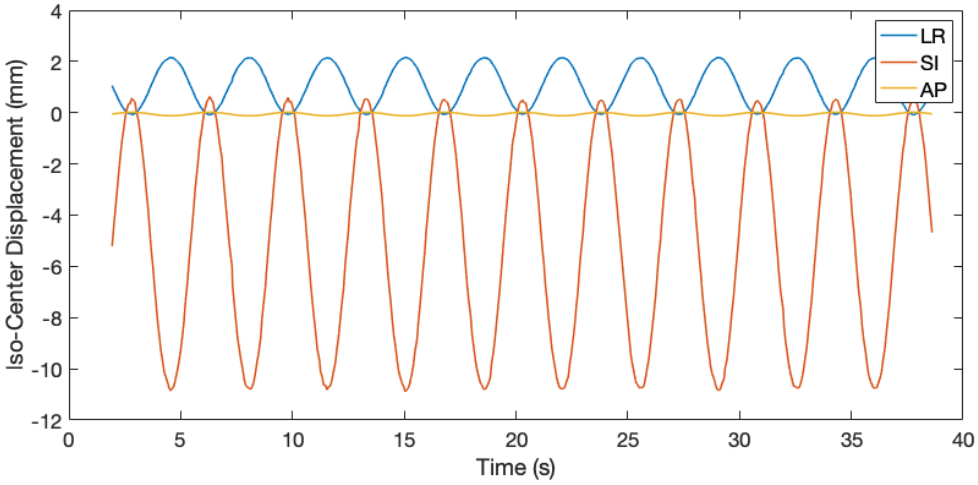

Figure 3-20. Location of the target sphere centroid calculated by the model for the respiratory phantom. The direction of the motion matches the true direction of the centroid motion along all three axes.

Table 3-2. The magnitude of the average and standard deviation of the displacement in each direction compared with the ground truth for respiratory phantom.

Respiratory Phantom	**Ground Truth (mm)**	**Model Results (mm)**	**Difference (mm)**
LR	2.77 ± 0.1	2.21 ± 0.01	0.56
AP	0.24 ± 0.1	0.14 ± 0.00	0.10
SI	10.00 ± 0.1	11.35 ± 0.06	1.35

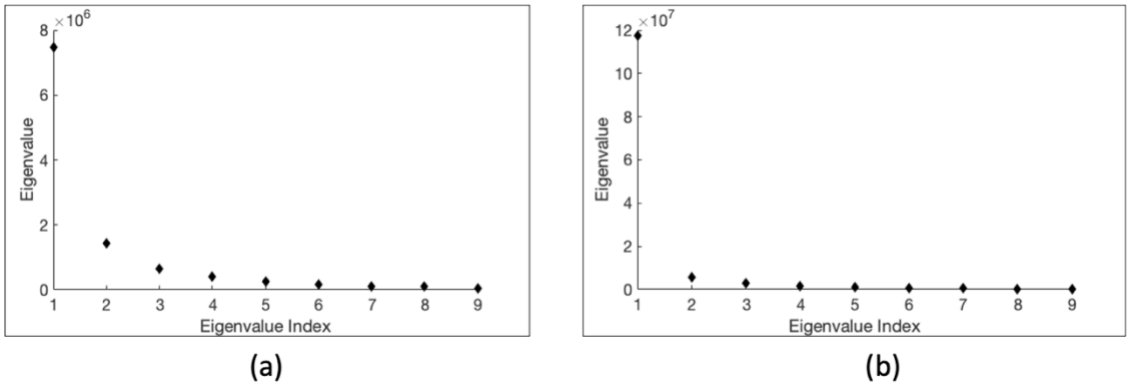

Figure 3-21. PCA eigenvalue spectrum for the respiratory phantom (a) and for patient no. 5 (b).

3.3.2. Patient Data

Figure 3-21.b shows the eigenvalue spectrum for one of the patients. For all patients, only the eigenvector associated with the largest eigenvalue was used to construct the correspondence model.

Figure 3-22 shows the location of the apex of the left diaphragm during part of the treatment for patient 5. The direction of the motion matches that of the diaphragm apex motion in 2D projections in all three directions. The magnitude of the average and standard deviation of the displacement in LR, AP, and SI directions are compared with the ground truth in tables 2.3, 2.4, and 2.5, respectively. Since the measurement of the ground truth in LR and AP directions are only possible in one of the complete respirations during CBCT acquisition, there is no calculated standard deviation for ground truth in these two directions. However, in the SI direction, the tumor center or the apex of the diaphragm could be located in several consecutive EE and EI projections. Therefore, the standard deviation was calculated for ground truth in SI direction. Table 3-5 shows the number of complete respirations that were used to measure the ground truth in SI direction for each patient.

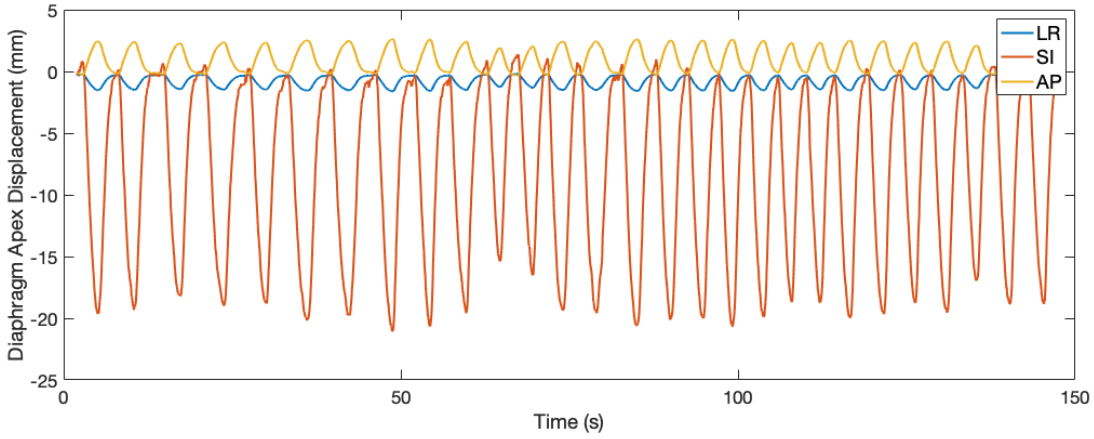

Figure 3-22. Location of the left diaphragm apex during the radiation delivery calculated by the model for patient no. 5 in the study.

For all patients, the error in the LR and AP directions is less than 1 mm (Table 3-3 and Table 3-4). In the SI direction, for all patients except patient 4, the error is less than 2 mm (Table 3-5). For patient 4, the error in SI direction is 3.13 mm. For patient 4, the average of the patient's skin displacement in all respiratory phases for secondary signal in 4DCT acquisition day was very close to the treatment day. However, for the primary signal, the average of the patient's skin displacement in all respiratory phases in treatment day was significantly larger than the 4DCT acquisition day. The fact that the primary signal was recorded larger on treatment day than the 4DCT acquisition day might be the reason for slightly larger error for this patient in SI direction. The results show that the model's accuracy is independent of the patient's type of breathing or irregularities.

Table 3-3. The average and standard deviation of the tumor center or diaphragm apex displacement during treatment in LR direction calculated by the model for each patient compared with the ground truth.

Patient	**Calculated Position**	**Ground Truth (mm)**	**Model Results (mm)**	**Difference (mm)**
1	Tumor Center	1.97	2.55 ± 0.60	0.58
2	Tumor Center	1.50	0.92 ± 0.10	0.58
3	Diaphragm Apex	1.05	1.17 ± 0.21	0.12
4	Diaphragm Apex	1.49	1.22 ± 0.19	0.27
5	Diaphragm Apex	1.83	1.16 ± 0.09	0.67

Table 3-4. The average and standard deviation of the tumor center or diaphragm apex displacement during treatment in AP direction calculated by the model for each patient compared with the ground truth.

Patient	Calculated Position	Ground Truth (mm)	Model Results (mm)	Difference (mm)
1	Tumor Center	0.57	0.57 ± 0.13	0.00
2	Tumor Center	6.66	6.31 ± 0.71	0.35
3	Diaphragm Apex	0.24	0.14 ± 0.00	0.10
4	Diaphragm Apex	1.24	0.96 ± 0.05	0.28
5	Diaphragm Apex	1.88	2.46 ± 0.19	0.58

Table 3-5. The average and standard deviation of the tumor center or diaphragm apex displacement during treatment in SI direction calculated by the model for each patient compared with the ground truth. Number of the respirations indicates the number of respirations used to calculate the ground truth. This is the number of all consecutive EE and EI projections for which the tumor center or the apex of the diaphragm was visible to the eyes.

Patient	Calculated Position	Ground Truth (mm)	No. of Respirations	Model Results (mm)	Difference (mm)
1	Tumor Center	4.22 ± 0.65	3	3.46 ± 0.80	0.76
2	Tumor Center	5.13 ± 0.93	7	5.40 ± 0.58	0.27
3	Diaphragm Apex	12.11 ± 2.47	9	12.55 ± 2.05	0.44
4	Diaphragm Apex	12.55 ± 2.81	7	15.68 ± 2.49	3.13
5	Diaphragm Apex	20.06 ± 2.35	6	18.55 ± 1.45	1.51

The systematic uncertainty of each step in the model construction is presented in Table 3-6. The systematic uncertainty for the Sentinel system is considered as the noise and drift error of the amplitude in the respiratory signal and depends on the patient's weight. For patients weighing between 69 to 91 kg, the estimated root mean square error (RMSE) for the Sentinel system is 0.5 mm [102]. In DIRART software, the registration accuracy of the Horn and Schunck algorithm is around 0.5-1.5 mm [98]. Here, to calculate the total uncertainty, the upper bound (1.5 mm) was employed as a conservative estimate. Finally, the RMSE of tracking accuracy of the CatalystHD system is 0.11-0.24 mm [103], and the upper bound (0.24 mm) was used in the calculation of the total uncertainty.

Table 3-6: Systematic uncertainty for each step of the model construction and the calculated total systematic uncertainty.

Uncertainty Source	RMSE (mm)
Sentinel	0.50
HS Image Registration Algorithm in DIRART	1.5
CatalystHD	0.241
Total	1.59

3.4. Discussion

This work describes the development of a patient-specific correspondence model to localize and track tumors in the thorax during radiation therapy. This model is constructed using 4DCT images of the patient and the displacement of two points on the patient's skin surface as the surrogate signals. The surface imaging system employed to record the surrogate signals is a dose-free and non-invasive technology without any special breathing instructions for the patients. Patients can breathe normally during both the 4DCT acquisition and treatment.

To construct the model, amplitude-sorted 4DCT images are used, which have several benefits. The amplitude-sorted algorithm does account for hysteresis and irregular breathing. Moreover, the amplitude-binning algorithm reduces the artifacts in 4DCT images. This improves the quality of internal motion datasets and, therefore, yields more precise image registration results. In general, image registration accuracy is an important component of the accuracy of the model.

The results of our study confirm that there is a correlation between external and internal anatomy motion, which is consistent with the results of studies performed by Chi et al. [82], Fayad et al. [104], and Beddar et al. [105].

Fassi et al. [79] proposed a patient-specific respiratory motion model derived from 4DCT images of the patient. In their model, parameters such as baseline, amplitude, and phase are updated at each treatment session using in-room radiography acquisition and optical surface imaging. For updating the baseline, the mid-position 4DCT image has to be registered with CBCT image, which has a lower quality than the 4DCT image, and that

affects the accuracy of the model. Also, using a deformable mesh registration algorithm for extracting the amplitude and phase from the surrogate signal is a time-consuming process and makes it hard to expand the model's application to real-time tracking. In our study, the EE phase is considered as reference (baseline). Therefore, the magnitude of the skin displacement is considered as the surrogate signal, and the model delivers the displacement of the anatomy of the interest with respect to the EE phase. Since recording of the surrogate signals with CatalystHD is simple and continuous there is a potential to expand the application of the model to real-time tracking.

Fayad et al. [106] developed a 4D global respiratory motion model to correlate the internal motion to patient's external surface motion. Their motion model is adapted on each patient by two static CT images (at full expiration and full inspiration), and patient's surface maps are extracted from either CT images or optical imaging devices. The evaluation of their model showed promising results for six patients. However, acquiring CT images at full expiration and full inspiration requires breath-hold technique, which is not possible for some patients [107].

The results of testing the model on a phantom and five patients showed a primary validation of our study. However, testing the model on a larger population of patients can examine the technique more precisely.

3.5. Conclusions

In this study, we developed a patient-specific correspondence model to locate the 3D position of the tumor or any other anatomy of interest in the thorax during radiation therapy. The localization error in both the LR and AP directions is less than 1 mm, and is less than 4 mm in the SI direction. The accuracy of results is independent of the patient's breathing type and irregularities.

Chapter 4

4.Summary and Future Work

4.1. Summary

The aim of this work was to find methods to reduce the impact of respiratory-induced motion in radiation therapy of lung cancer patients.

First, the application of combining stereotactic body frames with a surface imaging system for patient positioning in stereotactic body radiotherapy (SBRT) of lung cancer was evaluated. Combining the use of a surface imaging system with stereotactic body frames adds another level of accuracy to patient setup and provides monitoring of the movements during treatment. However, the presence of the compression plate and respiratory belt prevents the monitoring of respiratory signals.

In the second part of this work, a correspondence model was developed to track the tumors in the lung during radiation delivery. Based on previous studies, we assumed that there is a patient-specific correlation between the internal and external motion for each patient on the thoracic area. To find this correlation, two types of data were employed. First, 4DCT images acquired from the patient on the simulation day, and second, the displacement of two points on the patient's skin surface on the chest area as surrogate signals during 4DCT image acquisition. Image and signal processing procedures were applied to the acquired data to extract the internal and external motion data. PCA was used as a mathematical tool to fit the correspondence model on the internal and external motion data. The final result

is a patient-specific correspondence model that can calculate the location of the tumor during radiation delivery when receiving the surrogate signals as input.

The accuracy of the model was evaluated on a respiratory phantom and five lung cancer patients. The accuracy of the localization in LR and AP directions were less than 1 mm for both phantom and patient study. In the SI direction, the localization error was less than 2 mm for the phantom and less than 4 mm for all patients.

4.2. Future Work

The correspondence model presented in this work can localize any voxel in the volume selected for 4DCT acquisition. Therefore, its application can be expanded to localize tumors or any other anatomical structures of interest in the thorax or abdomen.

This model can be used for inter-fraction studies during which the patients' weight, anatomy, and type of breathing may change. The average, maximum, and minimum ranges of the tumor motion in all directions can be calculated by the model after each session and compared with previous sessions to see if there is any need to modify the treatment plan. Also, 4D CBCT images of the patients can be potentially constructed to update the model. Since the recording of the surrogate signals is continuous, the application of this model can be expanded to real-time tumor tracking. In that case, the time delay between recording the surrogate signals and calculation of the tumor location has to be assessed.

The results of testing the model made in this study showed a primary validation for localizing the tumors in the lung. Testing the model on a larger population of patients with more variety of breathing types and tumor locations will examine the accuracy of the localization more precisely.

Bibliography

[1] J. D. Bourland, Ed., *Image-Guided Radiation Therapy*. CRC Press, 2012.

[2] C. J. Ritchie, J. Hsieh, M. F. Gard, J. D. Godwin, Y. Kim, and C. R. Crawford, "Predictive respiratory gating: a new method to reduce motion artifacts on CT scans.," *Radiology*, vol. 190, no. 3, pp. 847–852, Mar. 1994, doi: 10.1148/radiology.190.3.8115638.

[3] J.-J. Sonke, L. Zijp, P. Remeijer, and M. van Herk, "Respiratory correlated cone beam CT," *Med. Phys.*, vol. 32, no. 4, pp. 1176–1186, Mar. 2005, doi: 10.1118/1.1869074.

[4] J. M. Balter, R. K. Ten Haken, T. S. Lawrence, K. L. Lam, and J. M. Robertson, "Uncertainties in CT-based radiation therapy treatment planning associated with patient breathing," *Int. J. Radiat. Oncol.*, vol. 36, no. 1, pp. 167–174, Aug. 1996, doi: 10.1016/S0360-3016(96)00275-1.

[5] A. E. Lujan, E. W. Larsen, J. M. Balter, and R. K. Ten Haken, "A method for incorporating organ motion due to breathing into 3D dose calculations," *Med. Phys.*, vol. 26, no. 5, pp. 715–720, May 1999, doi: 10.1118/1.598577.

[6] P. J. Keall *et al.*, "The management of respiratory motion in radiation oncology report of AAPM Task Group 76a)," *Med. Phys.*, vol. 33, no. 10, pp. 3874–3900, Sep. 2006, doi: 10.1118/1.2349696.

[7] J. R. van Sörnsen de Koste, F. J. Lagerwaard, H. C. . de Boer, M. R. . Nijssen-Visser, and S. Senan, "Are multiple CT scans required for planning curative radiotherapy in lung tumors of the lower lobe?," *Int. J. Radiat. Oncol.*, vol. 55, no. 5, pp. 1394–1399, Apr. 2003, doi: 10.1016/S0360-3016(02)04602-3.

[8] J. R. van Sörnsen de Koste *et al.*, "Dosimetric consequences of tumor mobility in

radiotherapy of stage I non-small cell lung cancer – an analysis of data generated using 'slow' CT scans," *Radiother. Oncol.*, vol. 61, no. 1, pp. 93–99, Oct. 2001, doi: 10.1016/S0167-8140(01)00373-5.

[9] F. J. Lagerwaard *et al.*, "Multiple 'slow' CT scans for incorporating lung tumor mobility in radiotheraphy planning," *Int. J. Radiat. Oncol.*, vol. 51, no. 4, pp. 932–937, Nov. 2001, doi: 10.1016/S0360-3016(01)01716-3.

[10] J. M. Balter, K. L. Lam, C. J. McGinn, T. S. Lawrence, and R. K. Ten Haken, "Improvement of CT-based treatment-planning models of abdominal targets using static exhale imaging," *Int. J. Radiat. Oncol.*, vol. 41, no. 4, pp. 939–943, Jul. 1998, doi: 10.1016/S0360-3016(98)00130-8.

[11] T. Aruga *et al.*, "Target volume definition for upper abdominal irradiation using CT scans obtained during inhale and exhale phases," *Int. J. Radiat. Oncol.*, vol. 48, no. 2, pp. 465–469, Sep. 2000, doi: 10.1016/S0360-3016(00)00610-6.

[12] S. S. Vedam, P. J. Keall, V. R. Kini, H. Mostafavi, H. P. Shukla, and R. Mohan, "Acquiring a four-dimensional computed tomography dataset using an external respiratory signal," *Phys. Med. Biol.*, vol. 48, no. 1, pp. 45–62, Jan. 2003, doi: 10.1088/0031-9155/48/1/304.

[13] E. C. Ford, G. S. Mageras, E. Yorke, and C. C. Ling, "Respiration-correlated spiral CT: A method of measuring respiratory-induced anatomic motion for radiation treatment planning," *Med. Phys.*, vol. 30, no. 1, pp. 88–97, Dec. 2002, doi: 10.1118/1.1531177.

[14] D. A. Low *et al.*, "A method for the reconstruction of four-dimensional synchronized CT scans acquired during free breathing," *Med. Phys.*, vol. 30, no. 6, pp. 1254–1263, May 2003, doi: 10.1118/1.1576230.

[15] G. S. Mageras *et al.*, "Measurement of lung tumor motion using respiration-correlated CT," *Int. J. Radiat. Oncol.*, vol. 60, no. 3, pp. 933–941, Nov. 2004, doi: 10.1016/j.ijrobp.2004.06.021.

[16] T. Pan, T.-Y. Lee, E. Rietzel, and G. T. Y. Chen, "4D-CT imaging of a volume influenced by respiratory motion on multi-slice CT," *Med. Phys.*, vol. 31, no. 2, pp. 333–340, Jan. 2004, doi: 10.1118/1.1639993.

[17] R. W. M. Underberg, F. J. Lagerwaard, B. J. Slotman, J. P. Cuijpers, and S. Senan, "Use of maximum intensity projections (MIP) for target volume generation in 4DCT scans for lung cancer," *Int. J. Radiat. Oncol.*, vol. 63, no. 1, pp. 253–260, Sep. 2005, doi: 10.1016/j.ijrobp.2005.05.045.

[18] V. R. Kini, S. S. Vedam, P. J. Keall, S. Patil, C. Chen, and R. Mohan, "Patient training in respiratory-gated radiotherapy," *Med. Dosim.*, vol. 28, no. 1, pp. 7–11, Mar. 2003, doi: 10.1016/S0958-3947(02)00136-X.

[19] P. J. Keall *et al.*, "Acquiring 4D thoracic CT scans using a multislice helical method," *Phys. Med. Biol.*, vol. 49, no. 10, pp. 2053–2067, May 2004, doi: 10.1088/0031-9155/49/10/015.

[20] S. S. Vedam, P. J. Keall, V. R. Kini, and R. Mohan, "Determining parameters for respiration-gated radiotherapy," *Med. Phys.*, vol. 28, no. 10, pp. 2139–2146, Oct. 2001, doi: 10.1118/1.1406524.

[21] R. I. Berbeco, S. Nishioka, H. Shirato, G. T. Y. Chen, and S. B. Jiang, "Residual motion of lung tumours in gated radiotherapy with external respiratory surrogates," *Phys. Med. Biol.*, vol. 50, no. 16, pp. 3655–3667, Aug. 2005, doi: 10.1088/0031-9155/50/16/001.

[22] J. Hanley *et al.*, "Deep inspiration breath-hold technique for lung tumors: the potential value of target immobilization and reduced lung density in dose escalation," *Int. J. Radiat. Oncol.*, vol. 45, no. 3, pp. 603–611, Oct. 1999, doi: 10.1016/S0360-3016(99)00154-6.

[23] D. Mah *et al.*, "Technical aspects of the deep inspiration breath-hold technique in the treatment of thoracic cancer," *Int. J. Radiat. Oncol.*, vol. 48, no. 4, pp. 1175–1185, Nov. 2000, doi: 10.1016/S0360-3016(00)00747-1.

[24] K. E. Rosenzweig *et al.*, "The deep inspiration breath-hold technique in the treatment of

inoperable non–small-cell lung cancer," *Int. J. Radiat. Oncol.*, vol. 48, no. 1, pp. 81–87, Aug. 2000, doi: 10.1016/S0360-3016(00)00583-6.

[25] V. M. Remouchamps *et al.*, "Initial clinical experience with moderate deep-inspiration breath hold using an active breathing control device in the treatment of patients with left-sided breast cancer using external beam radiation therapy," *Int. J. Radiat. Oncol.*, vol. 56, no. 3, pp. 704–715, Jul. 2003, doi: 10.1016/S0360-3016(03)00010-5.

[26] J. W. Wong *et al.*, "The use of active breathing control (ABC) to reduce margin for breathing motion," *Int. J. Radiat. Oncol.*, vol. 44, no. 4, pp. 911–919, Jul. 1999, doi: 10.1016/S0360-3016(99)00056-5.

[27] D. J. . Kim, B. R. Murray, R. Halperin, and W. H. . Roa, "Held-breath self-gating technique for radiotherapy of non–small-cell lung cancer: A feasibility study," *Int. J. Radiat. Oncol.*, vol. 49, no. 1, pp. 43–49, Jan. 2001, doi: 10.1016/S0360-3016(00)01372-9.

[28] E. A. Barnes, B. R. Murray, D. M. Robinson, L. J. Underwood, J. Hanson, and W. H. . Roa, "Dosimetric evaluation of lung tumor immobilization using breath hold at deep inspiration," *Int. J. Radiat. Oncol.*, vol. 50, no. 4, pp. 1091–1098, Jul. 2001, doi: 10.1016/S0360-3016(01)01592-9.

[29] C. Bergom, A. Currey, N. Desai, A. Tai, and J. B. Strauss, "Deep Inspiration Breath Hold: Techniques and Advantages for Cardiac Sparing During Breast Cancer Irradiation," *Front. Oncol.*, vol. 8, Apr. 2018, doi: 10.3389/fonc.2018.00087.

[30] J. S. Stromberg *et al.*, "Active breathing control (ABC) for Hodgkin's disease: reduction in normal tissue irradiation with deep inspiration and implications for treatment," *Int. J. Radiat. Oncol.*, vol. 48, no. 3, pp. 797–806, Oct. 2000, doi: 10.1016/S0360-3016(00)00681-7.

[31] V. M. Remouchamps, F. A. Vicini, M. B. Sharpe, L. L. Kestin, A. A. Martinez, and J. W. Wong, "Significant reductions in heart and lung doses using deep inspiration breath hold

with active breathing control and intensity-modulated radiation therapy for patients treated with locoregional breast irradiation," *Int. J. Radiat. Oncol.*, vol. 55, no. 2, pp. 392–406, Feb. 2003, doi: 10.1016/S0360-3016(02)04143-3.

[32] I. Lax, H. Blomgren, I. Näslund, and R. Svanström, "Stereotactic Radiotherapy of Malignancies in the Abdomen: Methodological aspects," *Acta Oncol. (Madr).*, vol. 33, no. 6, pp. 677–683, Jan. 1994, doi: 10.3109/02841869409121782.

[33] I. Lax, "Target Dose Versus Extratarget Dose in Stereotactic Radiosurgery," *Acta Oncol. (Madr).*, vol. 32, no. 4, pp. 453–457, Jan. 1993, doi: 10.3109/02841869309093624.

[34] H. Blomgren, I. Lax, I. Näslund, and R. Svanström, "Stereotactic High Dose Fraction Radiation Therapy of Extracranial Tumors Using An Accelerator: Clinical experience of the first thirty-one patients," *Acta Oncol. (Madr).*, vol. 34, no. 6, pp. 861–870, Jan. 1995, doi: 10.3109/02841869509127197.

[35] M. J. Murphy *et al.*, "Image-guided radiosurgery for the spine and pancreas," *Comput. Aided Surg.*, vol. 5, no. 4, pp. 278–288, 2000, doi: 10.1002/1097-0150(2000)5:4<278::AID-IGS6>3.0.CO;2-K.

[36] Q.-S. Chen, M. S. Weinhous, F. C. Deibel, J. P. Ciezki, and R. M. Macklis, "Fluoroscopic study of tumor motion due to breathing: Facilitating precise radiation therapy for lung cancer patients," *Med. Phys.*, vol. 28, no. 9, pp. 1850–1856, Sep. 2001, doi: 10.1118/1.1398037.

[37] M. J. Murphy and D. Pokhrel, "Optimization of an adaptive neural network to predict breathing," *Med. Phys.*, vol. 36, no. 1, pp. 40–47, Dec. 2008, doi: 10.1118/1.3026608.

[38] H. Shirato *et al.*, "Physical aspects of a real-time tumor-tracking system for gated radiotherapy," *Int. J. Radiat. Oncol.*, vol. 48, no. 4, pp. 1187–1195, Nov. 2000, doi: 10.1016/S0360-3016(00)00748-3.

[39] P. G. Seiler, H. Blattmann, S. Kirsch, R. K. Muench, and C. Schilling, "A novel tracking

technique for the continuous precise measurement of tumour positions in conformal radiotherapy," *Phys. Med. Biol.*, vol. 45, no. 9, pp. N103–N110, Sep. 2000, doi: 10.1088/0031-9155/45/9/402.

[40] J. M. Balter *et al.*, "Accuracy of a wireless localization system for radiotherapy," *Int. J. Radiat. Oncol.*, vol. 61, no. 3, pp. 933–937, Mar. 2005, doi: 10.1016/j.ijrobp.2004.11.009.

[41] Y. Seppenwoolde *et al.*, "Precise and real-time measurement of 3D tumor motion in lung due to breathing and heartbeat, measured during radiotherapy," *Int. J. Radiat. Oncol.*, vol. 53, no. 4, pp. 822–834, Jul. 2002, doi: 10.1016/S0360-3016(02)02803-1.

[42] G. Benchetrit, "Breathing pattern in humans: diversity and individuality," *Respir. Physiol.*, vol. 122, no. 2–3, pp. 123–129, Sep. 2000, doi: 10.1016/S0034-5687(00)00154-7.

[43] P. J. Keall, V. R. Kini, S. S. Vedam, and R. Mohan, "Motion adaptive x-ray therapy: a feasibility study," *Phys. Med. Biol.*, vol. 46, no. 1, pp. 1–10, Jan. 2001, doi: 10.1088/0031-9155/46/1/301.

[44] T. Neicu, H. Shirato, Y. Seppenwoolde, and S. B. Jiang, "Synchronized moving aperture radiation therapy (SMART): average tumour trajectory for lung patients," *Phys. Med. Biol.*, vol. 48, no. 5, pp. 587–598, Mar. 2003, doi: 10.1088/0031-9155/48/5/303.

[45] L. Papież, "The leaf sweep algorithm for an immobile and moving target as an optimal control problem in radiotherapy delivery," *Math. Comput. Model.*, vol. 37, no. 7–8, pp. 735–745, Apr. 2003, doi: 10.1016/S0895-7177(03)00081-5.

[46] L. Papież, "DMLC leaf-pair optimal control of IMRT delivery for a moving rigid target," *Med. Phys.*, vol. 31, no. 10, pp. 2742–2754, Sep. 2004, doi: 10.1118/1.1779358.

[47] S. Webb, "Quantification of the fluence error in the motion-compensated dynamic MLC (DMLC) technique for delivering intensity-modulated radiotherapy (IMRT)," *Phys. Med. Biol.*, vol. 51, no. 7, pp. L17–L21, Apr. 2006, doi: 10.1088/0031-9155/51/7/L01.

[48] C. Ozhasoglu and M. J. Murphy, "Issues in respiratory motion compensation during

external-beam radiotherapy," *Int. J. Radiat. Oncol.*, vol. 52, no. 5, pp. 1389–1399, Apr. 2002, doi: 10.1016/S0360-3016(01)02789-4.

[49] A. Schweikard, G. Glosser, M. Bodduluri, M. J. Murphy, and J. R. Adler, "Robotic motion compensation for respiratory movement during radiosurgery," *Comput. Aided Surg.*, vol. 5, no. 4, pp. 263–277, 2000, doi: 10.1002/1097-0150(2000)5:4<263::AID-IGS5>3.0.CO;2-2.

[50] Y. Kamino *et al.*, "Development of a four-dimensional image-guided radiotherapy system with a gimbaled X-ray head," *Int. J. Radiat. Oncol.*, vol. 66, no. 1, pp. 271–278, Sep. 2006, doi: 10.1016/j.ijrobp.2006.04.044.

[51] M. Nakamura *et al.*, "Dosimetric characterization of a multileaf collimator for a new four-dimensional image-guided radiotherapy system with a gimbaled x-ray head, MHI-TM2000a)," *Med. Phys.*, vol. 37, no. 9, pp. 4684–4691, Aug. 2010, doi: 10.1118/1.3480510.

[52] M. Hiraoka, T. Mizowaki, Y. Matsuo, M. Nakamura, and D. Verellen, "The gimbaled-head radiotherapy system: Rise and downfall of a dedicated system for dynamic tumor tracking with real-time monitoring and dynamic WaveArc," *Radiother. Oncol.*, vol. 153, pp. 311–318, Dec. 2020, doi: 10.1016/j.radonc.2020.07.002.

[53] T. BORTFELD, S. JIANG, and E. RIETZEL, "Effects of motion on the total dose distribution," *Semin. Radiat. Oncol.*, vol. 14, no. 1, pp. 41–51, Jan. 2004, doi: 10.1053/j.semradonc.2003.10.011.

[54] B. D. Milliken, S. J. Rubin, R. J. Hamilton, L. S. Johnson, and G. T. Y. Chen, "Performance of a video-image-subtraction-based patient positioning system," *Int. J. Radiat. Oncol.*, vol. 38, no. 4, pp. 855–866, Jul. 1997, doi: 10.1016/S0360-3016(97)00081-3.

[55] L. S. Johnson, B. D. Milliken, S. W. Hadley, C. A. Pelizzari, D. J. Haraf, and G. T. Y. Chen, "Initial clinical experience with a video-based patient positioning system," *Int. J. Radiat. Oncol.*, vol. 45, no. 1, pp. 205–213, Aug. 1999, doi: 10.1016/S0360-3016(99)00182-0.

[56] A. Brahme, P. Nyman, and B. Skatt, "4D laser camera for accurate patient positioning,

collision avoidance, image fusion and adaptive approaches during diagnostic and therapeutic procedures," *Med. Phys.*, vol. 35, no. 5, pp. 1670–1681, Apr. 2008, doi: 10.1118/1.2889720.

[57] T. Moser, S. Fleischhacker, K. Schubert, G. Sroka-Perez, and C. P. Karger, "Technical performance of a commercial laser surface scanning system for patient setup correction in radiotherapy," *Phys. Medica*, vol. 27, no. 4, pp. 224–232, Oct. 2011, doi: 10.1016/j.ejmp.2010.10.005.

[58] P. Alaei and G. Ding, Eds., *Image Guidance in Radiation Therapy: Techniques, Accuracy, and Limitations*. 2018.

[59] C. Bert, K. G. Metheany, K. Doppke, and G. T. Y. Chen, "A phantom evaluation of a stereo-vision surface imaging system for radiotherapy patient setup," *Med. Phys.*, vol. 32, no. 9, pp. 2753–2762, Aug. 2005, doi: 10.1118/1.1984263.

[60] P. J. Schöffel, W. Harms, G. Sroka-Perez, W. Schlegel, and C. P. Karger, "Accuracy of a commercial optical 3D surface imaging system for realignment of patients for radiotherapy of the thorax," *Phys. Med. Biol.*, vol. 52, no. 13, pp. 3949–3963, Jul. 2007, doi: 10.1088/0031-9155/52/13/019.

[61] F. Walter, P. Freislederer, C. Belka, C. Heinz, M. Söhn, and F. Roeder, "Evaluation of daily patient positioning for radiotherapy with a commercial 3D surface-imaging system (Catalyst^{TM})," *Radiat. Oncol.*, vol. 11, no. 1, p. 154, Dec. 2016, doi: 10.1186/s13014-016-0728-1.

[62] F. Stieler, F. Wenz, M. Shi, and F. Lohr, "A novel surface imaging system for patient positioning and surveillance during radiotherapy," *Strahlentherapie und Onkol.*, vol. 189, no. 11, pp. 938–944, Nov. 2013, doi: 10.1007/s00066-013-0441-z.

[63] S. S. Lo, B. S. Teh, J. J. Lu, and T. E. Schefter, Eds., *Stereotactic Body Radiation Therapy*. Berlin, Heidelberg: Springer Berlin Heidelberg, 2012.

[64] Y. Ueda, T. Teshima, H. Cárdenes, and I. J. Das, “Evaluation of initial setup errors of two immobilization devices for lung stereotactic body radiation therapy (SBRT),” *J. Appl. Clin. Med. Phys.*, vol. 18, no. 4, pp. 62–68, Jul. 2017, doi: 10.1002/acm2.12093.

[65] B. Murray, K. Forster, and R. Timmerman, “Frame-Based Immobilization and Targeting for Stereotactic Body Radiation Therapy,” *Med. Dosim.*, vol. 32, no. 2, pp. 86–91, Jun. 2007, doi: 10.1016/j.meddos.2007.01.005.

[66] S. Pallotta, L. Marrazzo, M. Ceroti, P. Silli, and M. Bucciolini, “A phantom evaluation of Sentinel ™ , a commercial laser/camera surface imaging system for patient setup verification in radiotherapy,” *Med. Phys.*, vol. 39, no. 2, pp. 706–712, Jan. 2012, doi: 10.1118/1.3675973.

[67] F. Stieler, F. Wenz, D. Scherrer, M. Bernhardt, and F. Lohr, “Clinical evaluation of a commercial surface-imaging system for patient positioning in radiotherapy,” *Strahlentherapie und Onkol.*, vol. 188, no. 12, pp. 1080–1084, Dec. 2012, doi: 10.1007/s00066-012-0244-7.

[68] O. Gopan and Q. Wu, “Evaluation of the Accuracy of a 3D Surface Imaging System for Patient Setup in Head and Neck Cancer Radiotherapy,” *Int. J. Radiat. Oncol.*, vol. 84, no. 2, pp. 547–552, Oct. 2012, doi: 10.1016/j.ijrobp.2011.12.004.

[69] T. Moser *et al.*, “Clinical Evaluation of a Laser Surface Scanning System in 120 Patients for Improving Daily Setup Accuracy in Fractionated Radiation Therapy,” *Int. J. Radiat. Oncol.*, vol. 85, no. 3, pp. 846–853, Mar. 2013, doi: 10.1016/j.ijrobp.2012.05.026.

[70] T. Harada *et al.*, “Real-time tumor-tracking radiation therapy for lung carcinoma by the aid of insertion of a gold marker using bronchofiberscopy,” *Cancer*, vol. 95, no. 8, pp. 1720–1727, Oct. 2002, doi: 10.1002/cncr.10856.

[71] D. Ionascu, S. B. Jiang, S. Nishioka, H. Shirato, and R. I. Berbeco, “Internal-external correlation investigations of respiratory induced motion of lung tumors,” *Med. Phys.*, vol.

34, no. 10, pp. 3893–3903, Sep. 2007, doi: 10.1118/1.2779941.

[72] M. Hoogeman, J.-B. Prévost, J. Nuyttens, J. Pöll, P. Levendag, and B. Heijmen, "Clinical Accuracy of the Respiratory Tumor Tracking System of the CyberKnife: Assessment by Analysis of Log Files," *Int. J. Radiat. Oncol.*, vol. 74, no. 1, pp. 297–303, May 2009, doi: 10.1016/j.ijrobp.2008.12.041.

[73] A. Schweikard, H. Shiomi, and J. Adler, "Respiration tracking in radiosurgery," *Med. Phys.*, vol. 31, no. 10, pp. 2738–2741, Sep. 2004, doi: 10.1118/1.1774132.

[74] H. Shirato *et al.*, "Feasibility of insertion/implantation of 2.0-mm-diameter gold internal fiducial markers for precise setup and real-time tumor tracking in radiotherapy," *Int. J. Radiat. Oncol.*, vol. 56, no. 1, pp. 240–247, May 2003, doi: 10.1016/S0360-3016(03)00076-2.

[75] J. R. McClelland, D. J. Hawkes, T. Schaeffter, and A. P. King, "Respiratory motion models: A review," *Med. Image Anal.*, vol. 17, no. 1, pp. 19–42, Jan. 2013, doi: 10.1016/j.media.2012.09.005.

[76] W. L. Smith and N. Becker, "Time delays and margins in gated radiotherapy," *J. Appl. Clin. Med. Phys.*, vol. 10, no. 3, pp. 140–154, Jun. 2009, doi: 10.1120/jacmp.v10i3.2896.

[77] J. R. McClelland, S. Webb, D. McQuaid, D. M. Binnie, and D. J. Hawkes, "Tracking 'differential organ motion' with a 'breathing' multileaf collimator: magnitude of problem assessed using 4D CT data and a motion-compensation strategy," *Phys. Med. Biol.*, vol. 52, no. 16, pp. 4805–4826, Aug. 2007, doi: 10.1088/0031-9155/52/16/007.

[78] H. Fayad *et al.*, "A patient specific respiratory model based on 4D CT data and a time of flight camera (TOF)," in *2009 IEEE Nuclear Science Symposium Conference Record (NSS/MIC)*, Oct. 2009, pp. 2594–2598, doi: 10.1109/NSSMIC.2009.5402012.

[79] A. Fassi, J. Schaerer, M. Fernandes, M. Riboldi, D. Sarrut, and G. Baroni, "Tumor Tracking Method Based on a Deformable 4D CT Breathing Motion Model Driven by an External

Surface Surrogate," *Int. J. Radiat. Oncol.*, vol. 88, no. 1, pp. 182–188, Jan. 2014, doi: 10.1016/j.ijrobp.2013.09.026.

[80] D. A. Low *et al.*, "Novel breathing motion model for radiotherapy," *Int. J. Radiat. Oncol.*, vol. 63, no. 3, pp. 921–929, Nov. 2005, doi: 10.1016/j.ijrobp.2005.03.070.

[81] J. R. McClelland *et al.*, "Inter-fraction variations in respiratory motion models," *Phys. Med. Biol.*, vol. 56, no. 1, pp. 251–272, Jan. 2011, doi: 10.1088/0031-9155/56/1/015.

[82] P.-C. M. Chi, P. Balter, D. Luo, R. Mohan, and T. Pan, "Relation of external surface to internal tumor motion studied with cine CT," *Med. Phys.*, vol. 33, no. 9, pp. 3116–3123, Aug. 2006, doi: 10.1118/1.2241993.

[83] J. D. P. Hoisak, K. E. Sixel, R. Tirona, P. C. F. Cheung, and J.-P. Pignol, "Correlation of lung tumor motion with external surrogate indicators of respiration," *Int. J. Radiat. Oncol.*, vol. 60, no. 4, pp. 1298–1306, Nov. 2004, doi: 10.1016/j.ijrobp.2004.07.681.

[84] J. Nasehi Tehrani, A. McEwan, and J. Wang, "Lung surface deformation prediction from spirometry measurement and chest wall surface motion," *Med. Phys.*, vol. 43, no. 10, pp. 5493–5502, Sep. 2016, doi: 10.1118/1.4962479.

[85] A. Khamene *et al.*, "Characterization of Internal Organ Motion Using Skin Marker Positions BT - Medical Image Computing and Computer-Assisted Intervention – MICCAI 2004," 2004, pp. 526–533.

[86] A. P. King, C. Buerger, and T. Schaeffter, "Cardiac Respiratory Motion Modelling by Simultaneous Registration and Modelling from Dynamic MRI Images BT - Biomedical Image Registration," 2010, pp. 222–233.

[87] S. Fahmi, F. F. J. Simonis, and M. Abayazid, "Respiratory motion estimation of the liver with abdominal motion as a surrogate," *Int. J. Med. Robot. Comput. Assist. Surg.*, vol. 14, no. 6, p. e1940, Dec. 2018, doi: 10.1002/rcs.1940.

[88] S. Park, R. Farah, S. M. Shea, E. Tryggestad, R. Hales, and J. Lee, "Simultaneous tumor

and surrogate motion tracking with dynamic MRI for radiation therapy planning," *Phys. Med. Biol.*, vol. 63, no. 2, p. 025015, Jan. 2018, doi: 10.1088/1361-6560/aaa20b.

[89] Q. Zhang *et al.*, "A patient-specific respiratory model of anatomical motion for radiation treatment planning," *Med. Phys.*, vol. 34, no. 12, pp. 4772–4781, Nov. 2007, doi: 10.1118/1.2804576.

[90] J. Martin, J. McClelland, B. Champion, and D. J. Hawkes, "Building Surrogate-Driven Motion Models from Cone-Beam CT via Surrogate-Correlated Optical Flow BT - Information Processing in Computer-Assisted Interventions," 2014, pp. 61–67.

[91] S. Ahn *et al.*, "A feasibility study on the prediction of tumour location in the lung from skin motion," *Br. J. Radiol.*, vol. 77, no. 919, pp. 588–596, Jul. 2004, doi: 10.1259/bjr/64800801.

[92] L. I. Cerviño, A. K. Y. Chao, A. Sandhu, and S. B. Jiang, "The diaphragm as an anatomic surrogate for lung tumor motion," *Phys. Med. Biol.*, vol. 54, no. 11, pp. 3529–3541, Jun. 2009, doi: 10.1088/0031-9155/54/11/017.

[93] I. T. Jolliffe, *Principal Component Analysis*. New York: Springer-Verlag, 2002.

[94] H. Li *et al.*, "Clinical evaluations of an amplitude-based binning algorithm for 4DCT reconstruction in radiation therapy," *Med. Phys.*, vol. 39, no. 2, pp. 922–932, Jan. 2012, doi: 10.1118/1.3679015.

[95] D. Yang, H. Li, D. A. Low, J. O. Deasy, and I. El Naqa, "A fast inverse consistent deformable image registration method based on symmetric optical flow computation," *Phys. Med. Biol.*, vol. 53, no. 21, pp. 6143–6165, Nov. 2008, doi: 10.1088/0031-9155/53/21/017.

[96] B. K. P. Horn and B. G. Schunck, "Determining optical flow," *Artif. Intell.*, vol. 17, no. 1–3, pp. 185–203, Aug. 1981, doi: 10.1016/0004-3702(81)90024-2.

[97] D. Yang, W. Lu, D. A. Low, J. O. Deasy, A. J. Hope, and I. El Naqa, "4D-CT motion estimation using deformable image registration and 5D respiratory motion modeling," *Med.*

Phys., vol. 35, no. 10, pp. 4577–4590, Sep. 2008, doi: 10.1118/1.2977828.

[98] D. Yang *et al.*, "Technical Note: DIRART - A software suite for deformable image registration and adaptive radiotherapy research," *Med. Phys.*, vol. 38, no. 1, pp. 67–77, Dec. 2010, doi: 10.1118/1.3521468.

[99] L. Zijp, J. J. Sonke, and M. Herk, *Extraction of the Respiratory Signal from Sequential Thorax Cone-Beam X-Ray Images*. 2004.

[100] A. Kavanagh, P. M. Evans, V. N. Hansen, and S. Webb, "Obtaining breathing patterns from any sequential thoracic x-ray image set," *Phys. Med. Biol.*, vol. 54, no. 16, pp. 4879–4888, Aug. 2009, doi: 10.1088/0031-9155/54/16/003.

[101] R. Li *et al.*, "3D tumor localization through real-time volumetric x-ray imaging for lung cancer radiotherapy," *Med. Phys.*, vol. 38, no. 5, pp. 2783–2794, May 2011, doi: 10.1118/1.3582693.

[102] C. Heinz, M. Reiner, C. Belka, F. Walter, and M. Söhn, "Technical evaluation of different respiratory monitoring systems used for 4D CT acquisition under free breathing," *J. Appl. Clin. Med. Phys.*, vol. 16, no. 2, pp. 334–349, Mar. 2015, doi: 10.1120/jacmp.v16i2.4917.

[103] L. Chen *et al.*, "Accuracy of real-time respiratory motion tracking and time delay of gating radiotherapy based on optical surface imaging technique," *Radiat. Oncol.*, vol. 15, no. 1, p. 170, Dec. 2020, doi: 10.1186/s13014-020-01611-6.

[104] H. Fayad, T. Pan, J. François Clement, and D. Visvikis, "Technical Note: Correlation of respiratory motion between external patient surface and internal anatomical landmarks," *Med. Phys.*, vol. 38, no. 6Part1, pp. 3157–3164, May 2011, doi: 10.1118/1.3589131.

[105] A. S. Beddar *et al.*, "Correlation between internal fiducial tumor motion and external marker motion for liver tumors imaged with 4D-CT," *Int. J. Radiat. Oncol.*, vol. 67, no. 2, pp. 630–638, Feb. 2007, doi: 10.1016/j.ijrobp.2006.10.007.

[106] H. Fayad, M. Gilles, T. Pan, and D. Visvikis, "A 4D global respiratory motion model of the

thorax based on CT images: A proof of concept," *Med. Phys.*, vol. 45, no. 7, pp. 3043–3051, Jul. 2018, doi: 10.1002/mp.12982.

[107] S. B. Gay, C. L. Sistrom, C. A. Holder, and P. M. Suratt, "Breath-holding capability of adults. Implications for spiral computed tomography, fast-acquisition magnetic resonance imaging, and angiography.," *Invest. Radiol.*, vol. 29, no. 9, pp. 848–51, Sep. 1994, [Online]. Available: http://www.ncbi.nlm.nih.gov/pubmed/7995705.

Appendix A

The contours of the tumor on the 2D CBCT projections of patients 1 and 2 at EI and EE phases that the tumor was visible.

Patient 1:

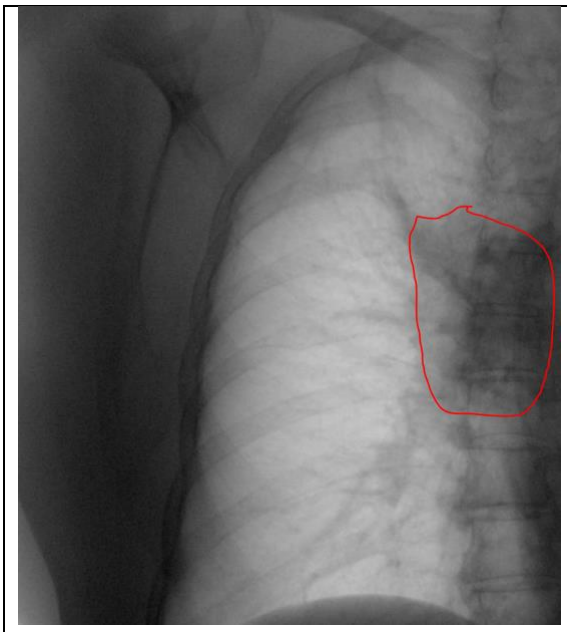	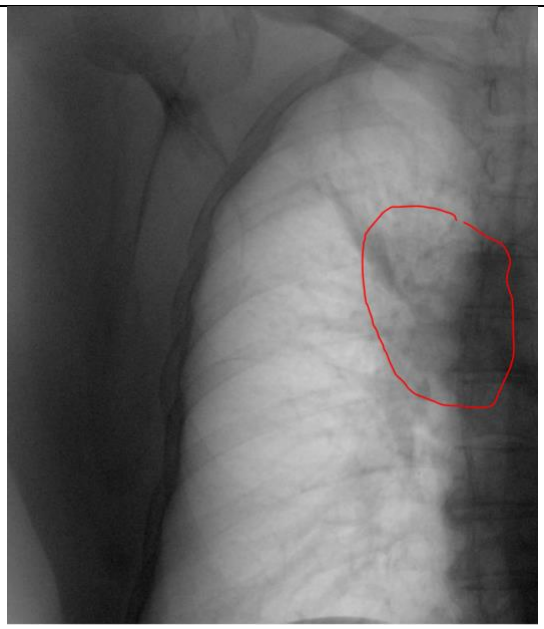
Projection 633 - EE	Projection 646 - EI

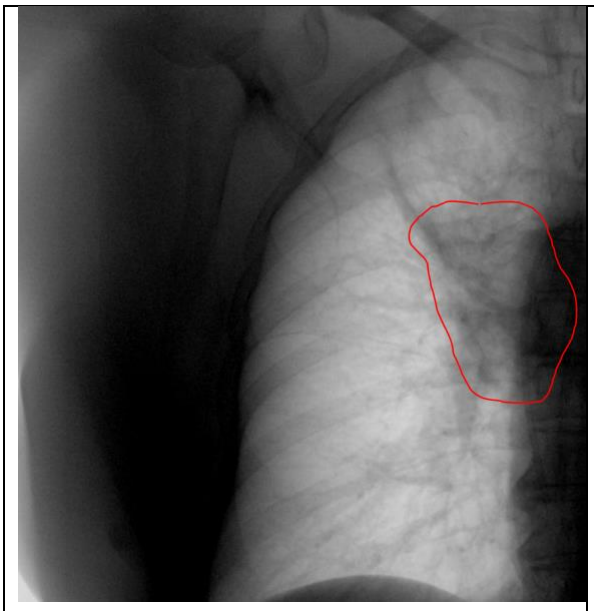

Projection 666 - EE

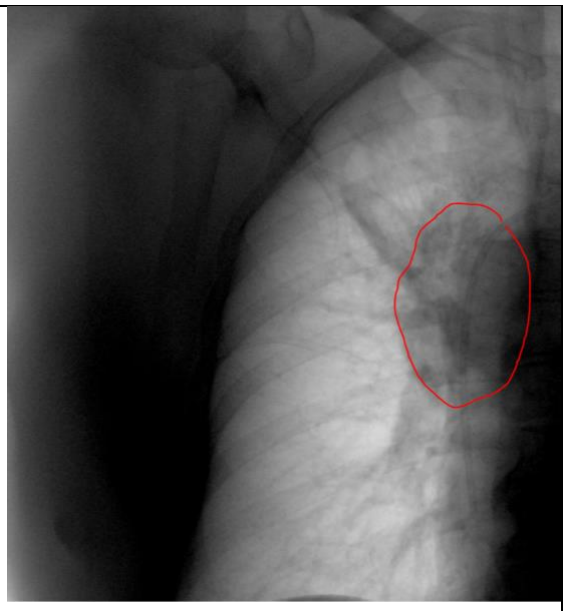

Projection 679 - EI

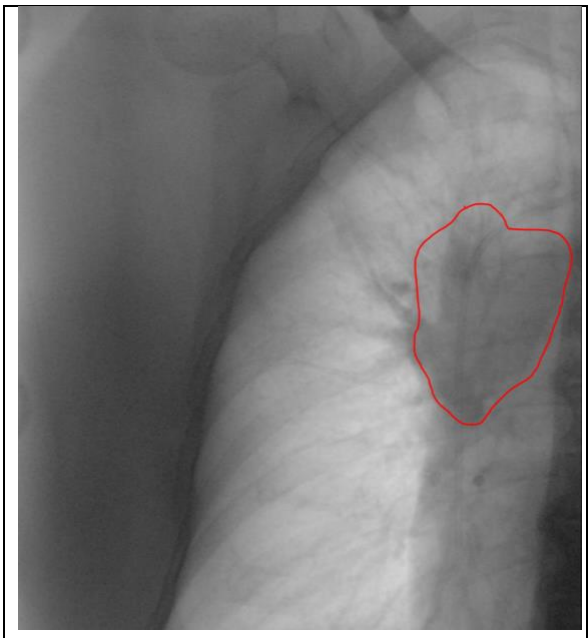

Projection 709 - EE

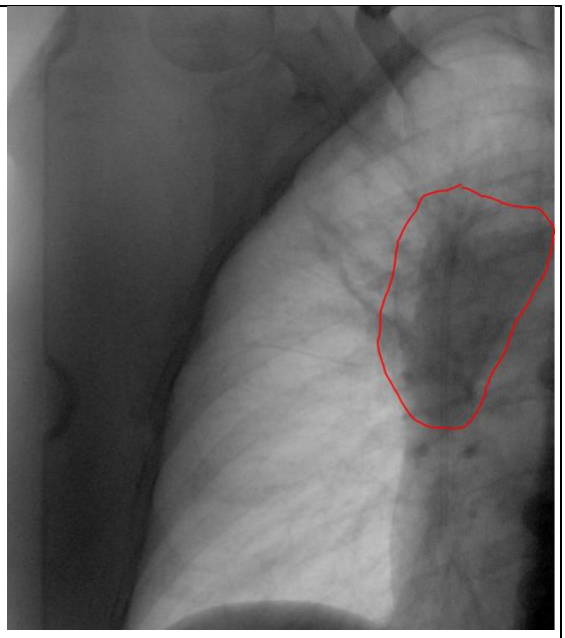

Projection 728 - EI

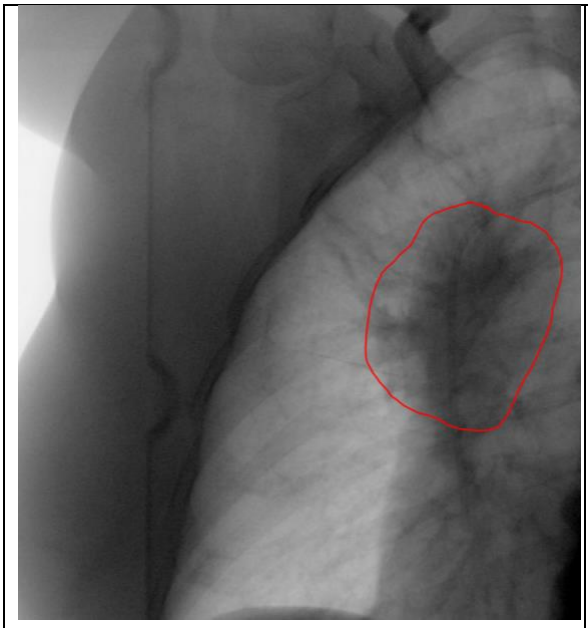	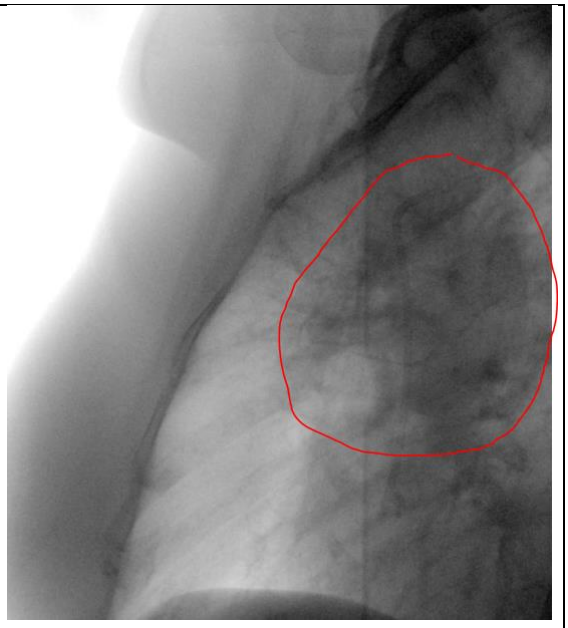
Projection 741 - EE	Projection 787 - EI

Patient 2:

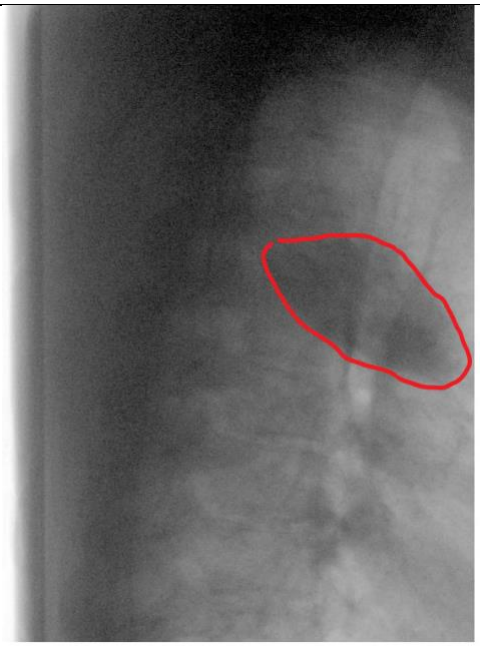

Projection 438 - EE

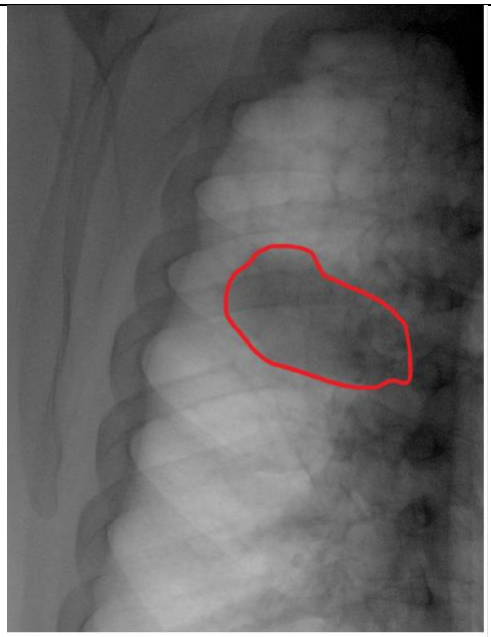

Projection 544 - EI

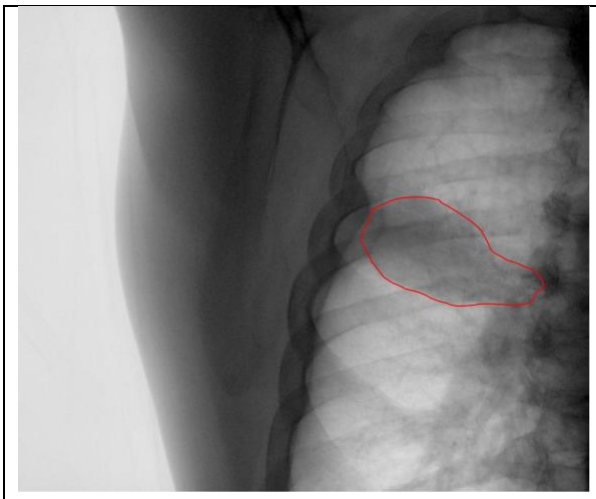

Projection 592 - EE

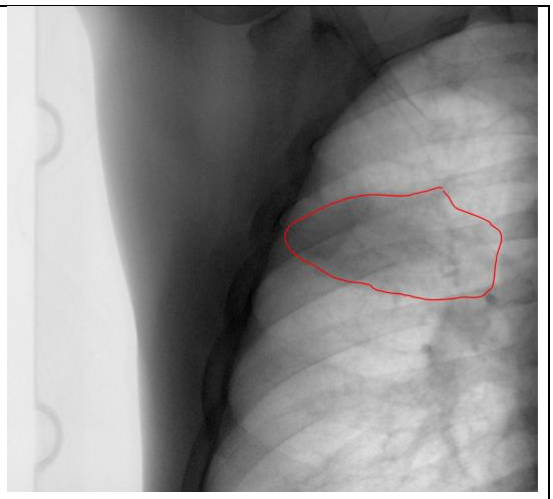

Projection 687 - EI

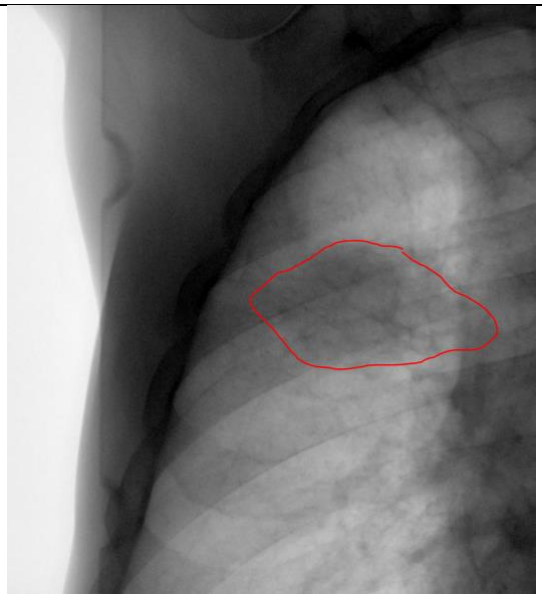

Projection 733 - EE

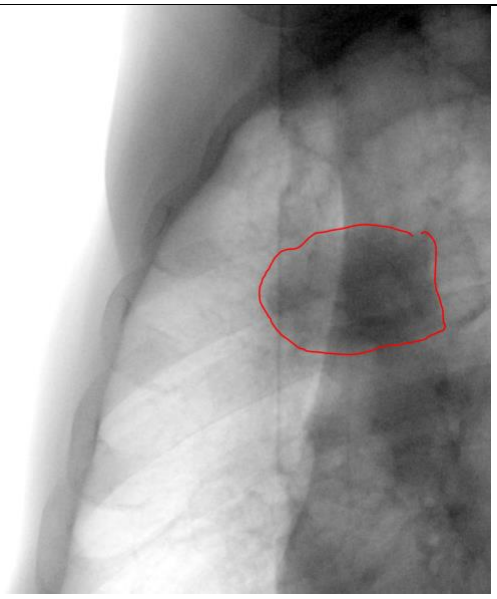

Projection 790 - EI

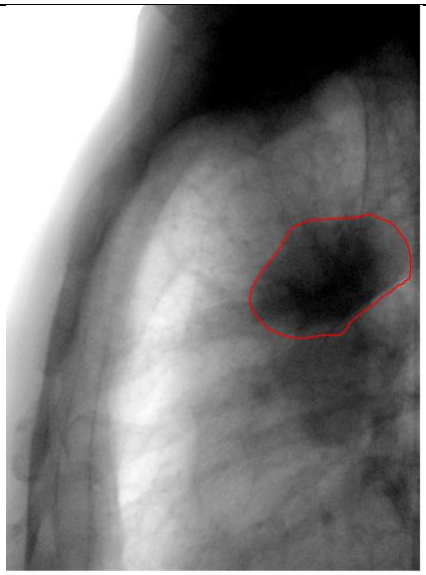

Projection 839 - EE

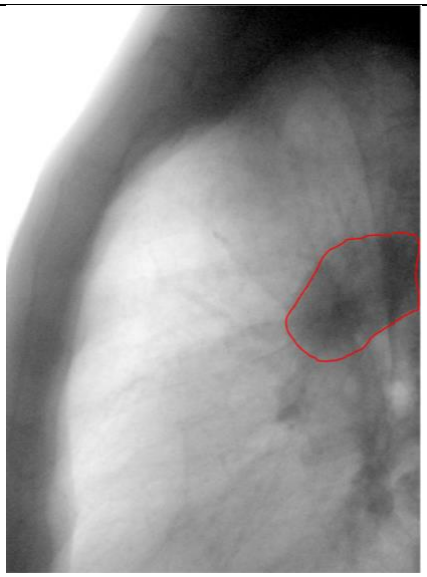

Projection 874 - EI